UNIVERSIDADE FEDERAL DE PERNAMBUCO
DEPARTAMENTO DE FÍSICA – CCEN
PROGRAMA DE PÓS-GRADUAÇÃO EM FÍSICA

ALEXANDRE ANDRADE CAVALCANTI DE ALMEIDA

SPECTRAL ANALYSIS OF THE FOUR-WAVE MIXING IN A COLD ATOMIC SAMPLE USING A SINGLE CW LASER

Recife
2019

ALEXANDRE ANDRADE CAVALCANTI DE ALMEIDA

SPECTRAL ANALYSIS OF THE FOUR-WAVE MIXING IN A COLD ATOMIC SAMPLE USING A SINGLE CW LASER

Dissertação apresentada ao Programa de Pós-Graduação em Física da Universidade Federal de Pernambuco, como requisito parcial para a obtenção do título de Mestre em Física.

Área de concentração: Óptica

Orientadora: Profa. Sandra Sampaio Vianna

Recife
2019

Catalogação na fonte
Bibliotecária Elaine Freitas CRB4-1790

A447s Almeida, Alexandre Andrade Cavalcanti de
Spectral analysis of the four-wave mixing in a cold atomic sample using a single CW laser / Alexandre Andrade Cavalcanti de Almeida . – 2019.
65 f.: fig.

Orientadora: Sandra Sampaio Vianna
Dissertação (Mestrado) – Universidade Federal de Pernambuco. CCEN. Física. Recife, 2019.
Inclui referências.

1. Óptica 2. Mistura de quatro ondas. 3. Átomos frios. 4. Espectroscopia. I. Vianna, Sandra Sampaio (orientadora). II. Título.

535.2 CDD (22. ed.) UFPE-FQ 2019-20

ALEXANDRE ANDRADE CAVALCANTI DE ALMEIDA

SPECTRAL ANALYSIS OF THE FOUR-WAVE MIXING IN A COLD ATOMIC SAMPLE USING A SINGLE CW LASER

Dissertação apresentada ao Programa de Pós-Graduação em Física da Universidade Federal de Pernambuco, como requisito parcial para a obtenção do título de Mestre em Física.

Aprovada em: 20/02/2019.

BANCA EXAMINADORA

_____

Profa. Sandra Sampaio Vianna
Orientadora
Universidade Federal de Pernambuco

_____

Prof. José Wellington Rocha Tabosa
Examinador Interno
Universidade Federal de Pernambuco

_____

Prof. Tommaso Macri
Examinador Externo
Universidade Federal do Rio Grande do Norte

AGRADECIMENTOS

Aos meus pais Evângela Andrade e Antônio Carlos Almeida, que me apoiaram incondicionalmente em todos os momentos de minha formação e a todos familiares, em especial meu irmão Mário Jorge Andrade que mesmo com a pouca idade muito me ajudou. À minha namorada Mariana Pessoa, por me acompanhar desde muito antes da física entrar na minha vida e sem a qual eu não seria quem eu sou.

À professora Sandra Vianna, pela orientação de muitos anos e por te me ensinado como fazer pesquisa. À professora Marta Bibiano, por ter sugerido e incentivado a física como uma carreira para mim. Hoje não me imagino fazendo outra coisa.

Aos colegas de laboratório, em especial Natalia de Melo e Alexis García-Wong, por todas as discussões e conselhos e principalmente, por serem meus amigos.

Agradeço a todos aqueles que desempenharam os mais diversos papéis para a conclusão deste trabalho, de forma direta ou indireta.

Por fim, agradeço ao CNPq pelo apoio financeiro.

ABSTRACT

We describe an experimental and theoretical study of the four-wave mixing spectrum in ^{87}Rb atoms trapped in a magneto-optical trap. Our experimental setup uses a single cw laser to produce two copropagating beams inducing two identical four-wave mixing processes. The initial goal of the work was to analyze and compare these two signals, looking for what information they could give about the atomic system. However, since a single spectrum presents an unexpected valley around the resonance, we will focus the analyses and theoretical modelling in explaining this feature. In order to explain the nature of this valley, we performed several series of measurements, changing parameters such as laser intensity or optical depth of the sample. To interpret the experimental results our theoretical model consists of a simple four-level N-shaped system. We write the Bloch equations and solve them considering the lowest order solution. Four excitation routes arise from this solution, but only the direct excitation route to the four-wave mixing process seems to agree partially with the experimental data. To improve the agreement, we add the absorption of the input beams and of the generated light. Therefore, our model gives evidence that the valley is due to a dispersion in a high intensity regime and to absorption effects for a low intensity regime. We discuss in further details the successes and failures of this model as well as a few options to achieve better descriptions.

Key-words: Four-wave mixing. Cold atoms. Nonlinear optics. Spectroscopy.

RESUMO

Neste trabalho apresentamos um estudo experimental e teórico da resposta espectral do sinal gerado no processo de mistura de quatro ondas em átomos de ^{87}Rb presos numa armadilha magneto-ótica. Utiliza-se um único laser *cw* para produzir dois feixes co-propagantes, induzindo dois processos de mistura de quatro ondas idênticos. O objetivo inicial do trabalho era analisar e comparar esses dois sinais, buscando quais informações poderiam ser extraídas sobre o sistema atômico. No entanto, como um espectro isolado apresenta um vale inesperado, realizamos uma série de medidas experimentais, variando parâmetros como a intensidade dos lasers ou a densidade ótica da amostra visando explicar este espectro de excitação. Para interpretar estes resultados experimentais, nosso modelo teórico consiste em um sistema tipo N de quatro níveis. As equações de Bloch são montadas e resolvidas considerando a solução de mais baixa ordem. Desta solução emergem quatro rotas de excitação, sendo apenas a rota de excitação direta para a mistura de quatro ondas capaz de explicar parcialmente os dados experimentais. Para melhorar a concordância com o experimento, adicionamos efeitos de absorção dos feixes de entrada e da luz gerada. Desta forma, nosso modelo fornece evidências de que o vale no espectro é resultado de uma dispersão para o regime de alta intensidade e da absorção dos feixes de entrada no regime de baixa intensidade. Procuramos discutir em detalhes os sucessos e fracassos do modelo bem como algumas opções para obter uma melhor descrição.

Palavras-chaves: Mistura de quatro ondas. Átomos frios. Ótica não-linear. Espectroscopia.

LISTA DE FIGURAS

SUMÁRIO

1 INTRODUCTION

Since the early days of laser cooling techniques [1] there has been a great interest in investigating nonlinear effects in cold atomic samples. This intersection of research topics has proved to be very fruitful, with works published on several topics such as the experimental realization of four-wave mixing with matter waves [2], the generation of correlated photon pairs [3], the study of cold Rydberg atoms [4] or nonlinear optical memories [5], to give some recent examples. These works correlate in some level with topics of interest to our research, in a more direct way or even being a future perspective, as it is in the case of Rydberg atoms or the use of atomic nonlinearities in quantum information experiments.

In the context of this intersection, we present experimental and theoretical results of a four-wave mixing (FWM) process in a cold ^{87}Rb sample. This nonlinear optical phenomenon is a powerful tool to understand more about the fundamental physics of atomic systems. Given that, the original goal of our research was to induce two simultaneous FWM processes and look for possible correlations between them, focusing on the informations that could be extracted about the atoms. However, as it will be discussed, the study of a single FWM spectrum has presented unexpected features, changing the focus of the work. Therefore, explaining these features is our main objective.

To provide some theoretical background, we describe briefly the FWM process and also the elements of the magneto-optical trap (MOT) in the following sections of this first chapter. It is important to describe the MOT, since it is the main apparatus of the experimental setup, being responsible for cooling and trapping the atoms.

In chapter 2, we present our experimental setups in details. More specifically, we show the components of our MOT, e.g. vacuum system, lasers and some characterization procedures. Furthermore, we describe the setup built to induce the FWM process as well as the specific measurement techniques and their temporal control. The reasoning behind the parameters of the experiment is also discussed.

It is in chapter 3 that we present all the experimental results. The chapter is divided in six sections, each one focusing on the behavior of the FWM signal in face of different parameters or experimental situations. In all of these results there are unexpected experimental features that are, to best of our knowledge, not described in the literature. It is possible through the analyses of the results to support or discard some hypotheses to explain the underlying physical mechanisms.

However, to properly interpret these features, a theoretical model is necessary. In chapter 4, we present our model alongside with some theoretical results and comparisons with the experiment. It is possible then to achieve a description of the phenomena that lead to the spectral characteristcs seen in the FWM process. We discuss some improvements or extra considerations

to the model, in order to increase the agreement with the experimental results. Finally, we present the conclusions and perspectives of this work.

1.1 Four-wave mixing

Optical wave mixing is a field of nonlinear optics with elevated and continuous research activity since the invention of the laser almost sixty years ago by Maiman [6]. In fact, only a year after Maiman's work, Franken *et al* [7] achieved second-harmonic generation with a Ruby laser, a work regarded by many as the beginning of nonlinear optics. To be fair, there were several nonlinear optics works in the early twentieth century using DC fields, but it was with the advent of the laser that the field truly expanded.

In the next few years a series of observations and techniques were published, such as the two-photon absorption by Kaiser and Garret [8], the stimulated Raman scattering by Woodbury and Ng [9] or the third-harmonic generation by Maker and Terhune [10]. These works and the subsequent ones allowed, for instance, measurements of energy structure, nonlinear susceptibilities and level lifetimes, in many different materials.

The area grown so quickly that in 1981 Nicholas Bloembergen and Arthur Schawlow received half of the Nobel prize in physics [11] for their contributions to laser spectroscopy, especially with the use of nonlinear optics techniques. Nowadays, the field remains very active, with researches ranging from quantum phenomena such as interference [12] or entanglement [13] to biology applications [14].

To understand these physical processes, we must first describe what is an optical nonlinearity. This description begins with the response of a medium to the action of light [15], i.e. the polarization

$$\vec{P} = \varepsilon_0 \chi \vec{E}, \tag{1}$$

where ε_0 is the vacuum permittivity, χ is the electric susceptibility and $\vec{E}$ is the electric field. We may consider that the response of the medium is entirely due to the electric field because of the small amplitude of the magnetic field of light.

It is in the polarization that the nonlinear phenomena manifest, i.e. when the electric field is strong enough to drive medium responses of higher orders. If that is the case, then the polarization might be expanded in the power series

$$\vec{P} = \varepsilon_0[\chi^{(1)}\vec{E} + \chi^{(2)}\vec{E}\vec{E} + \chi^{(3)}\vec{E}\vec{E}\vec{E} + \cdots], \tag{2}$$

where $\chi^{(2)}$ and $\chi^{(3)}$ are the second- and third-order nonlinear susceptibilities, and so on. Given the vector nature of the electric field, these susceptibilities must be tensors. For instance, $\chi^{(3)}$ is a fourth-rank tensor with 81 components, with each one of these consisting of a sum of several terms. Naturally, symmetries of the medium are often used to reduce the complexity of these tensors.

Typically, even-order processes have different restrictions than odd-order processes. For example, even-order processes cannot happen within centrosymmetric media, such as an atomic vapor. Therefore, in this particular work, we are interested only in third-order phenomena because it is the lowest order optical nonlinearity of a cold atomic sample. Furthermore, we focus on the FWM process.

To understand the FWM phenomenon, let us start with a general case of a third-order nonlinear optical process. Since there is a cubic dependency on the electric field, the most general case is a field with three spectral components

$$E(t) = E_1 e^{-i\omega_1 t} + E_2 e^{-i\omega_2 t} + E_3 e^{-i\omega_3 t} + c.c.. \tag{3}$$

Where we neglected the vector nature of the field and its spatial dependency to simplify the description. These three fields are able to induce polarization that rely on different mixing of frequencies. In fact there are 44 different possible frequency components of the polarization but, usually, the experimental setups are built to allow the observation of a particular component, e.g. exploring resonances of the material. The FWM itself is often described by the component

$$P(\omega_1 - \omega_2 + \omega_3) = 6\varepsilon_0 \chi^{(3)} E_1 E_2^* E_3. \tag{4}$$

This polarization term generates a fourth field with frequency $\omega_4 = \omega_1 - \omega_2 + \omega_3$ due to energy conservation. That is the origin of the name four-wave mixing. This new field is generated because a time-varying polarization can act as a source of electric field, as shown by the wave equation derived from the Maxwell's equations

$$\nabla^2 E - \frac{n^2}{c^2}\frac{\partial^2 E}{\partial t^2} = \frac{1}{\varepsilon_0 c^2}\frac{\partial^2 P(\omega_4)}{\partial t^2}, \tag{5}$$

where n is the index of refraction. In section 4.3 we actually solve this equation using a modeled polarization.

An example of how three fields combined may generate a fourth one in a two-level atom is shown in the scheme of Fig. 1. In this case, the FWM is degenerate since all four fields have the same frequencies. This setup is useful for this work, since the FWM described later is also degenerate.

To describe such quantum systems, it is often used the density-matrix formalism. With this formalism it is possible to model the coherences induced in the medium by the fields and connect them with the polarization. In the case of Fig. 1 the first input field induces a coherence between ground and excited state that oscillates with ω_1. If there was this single field, this coherence could only induce a linear polarization $P(\omega_1)$ (or a third-harmonic generation, with fields strong enough). The addition of the other two fields allows a coherence that oscillates with $\omega_4 = \omega_1 - \omega_2 + \omega_3$ and thus induces a polarization with the same frequency, acting as a source of the generated FWM light. Therefore the whole process can be summarized by the absorption of a

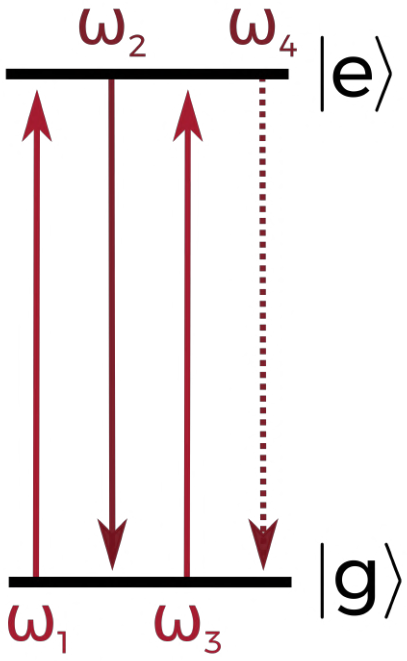

Figure 1 – Degenerate four-wave mixing in a two-level system.

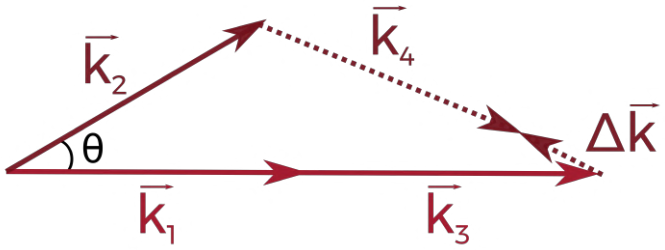

Figure 2 – Wavevectors for a FWM configuration with an angle between input fields.

photon, a stimulated emission followed by a second absorption inducing a coherence responsible for the generation of a fourth photon.

Finally, if one takes into account the spatial dependency of the fields, phase matching conditions arise. These conditions are natural consequences of Eq. (5) and of momentum conservation, i.e. $\vec{k}_4 = \vec{k}_1 - \vec{k}_2 + \vec{k}_3$. Due to changes in the index of refraction near resonances of the medium, this condition might only be satisfied if there is an angle between wavevectors, as shown in Fig. 2, where $\Delta\vec{k} = \vec{k}_1 - \vec{k}_2 + \vec{k}_3 - \vec{k}_4$.

In the expression of the intensity of the FWM light, the phase matching typically appears as a modulation with the functional form $sinc^2(\Delta kL)$. Therefore, the phase mismatch must be small, otherwise the *sinc* function will considerably weaken the signal. For experimental conditions, this implies that the angle between input fields, as shown in Fig. 2, must be small. This angle might also exist in order to allow spatial separation of the input and generated fields,

as it is the case of this work.

1.2 Magneto-optical trap

One of the main complications of studying atoms using light is dealing with effects caused by their movement. To manage this, several techniques, such as saturated absorption spectroscopy [16] or two-photon absorption [8], were developed in the past years. But these techniques are only clever workarounds to eliminate the Doppler effect. Perhaps, a more straightforward approach of the problem would be to eliminate, or at least weaken, the atomic movement. In view of this, we describe how lasers can be used to slow down atoms and how this is applied in magneto-optical traps, a technique used in many atom trapping experiments nowadays. The development of these laser cooling and trapping experiments led to 1997 Nobel prize, awarded to Steven Chu, Claude Cohen-Tannoudji and William Philips [17].

It is a well known fact that light carries linear momentum. Given that, when a photon interacts with a moving atom there might be a momentum transference if the atom absorbs the photon. The force exerted in this phenomenon is the radiation force [18]

$$F = \frac{\sigma_{abs} I}{c}, \tag{6}$$

where σ_{abs} is the peak absorption cross-section of the atom, I is the laser intensity and c is the light velocity in vacuum. Usually, for the resonance frequency, this peak absorption cross-section is much larger than the actual size of the atom making the radiation force quite significant.

Even though this description of the force does not need to consider a quantized light, it is insightful to look at the problem in such way. Each photon absorbed by the atoms must be re-emitted by spontaneous emission in a random direction. Hence, the whole process can be seen as a scattering of photons. The force in this case is given by the multiplication of the photon momentum $\hbar k$ and the scattering rate. If we consider a two-level atom as model, then this force is [18]

$$F_{scatt} = \hbar k \frac{\Gamma}{2} \frac{I/I_{sat}}{1 + I/I_{sat} + 4\delta^2/\Gamma^2}, \tag{7}$$

where Γ is the decay rate of the excited state, I_{sat} is the saturation intensity and δ is the detuning from resonance. For a moving atom, we might already take into account the Doppler effect, i.e. $\delta = \omega - \omega_0 + kv$, where ω is the laser frequency, ω_0 is the resonance frequency, k is the wavevector and v is the atomic velocity.

With Eq. (7) in hand, we can understand the optical molasses technique developed by Chu *et al* in 1985 [19]. Still with the simple model of a two-level atom, consider the interaction with a pair of counter-propagating lasers, as presented in Fig. 3.

Since the atoms are moving in the direction of propagation of light, there will be a shift in the frequency of the lasers as seen by the atoms, caused by the Doppler effect. It is possible

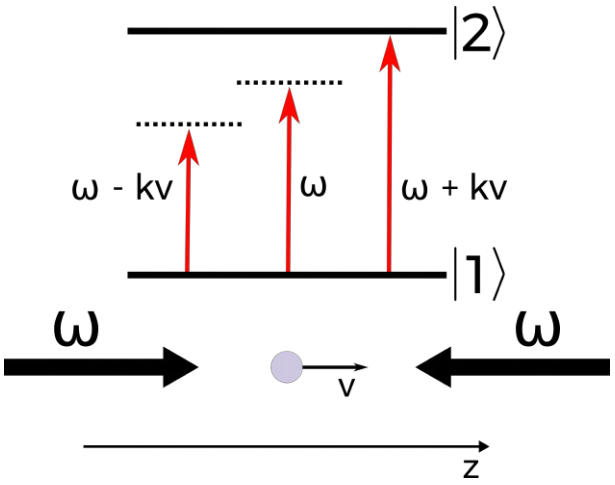

Figure 3 – Optical molasses technique: counter-propagating lasers acting on a moving two-level atom.

then, to choose the correct detuning to make one of the lasers resonant with a certain velocity group, leading to an absorption. Only these atoms will be slowed.

Let us try to see the behavior of the combined forces in this situation. The net force on the atom is

$$F_{molasse} = F_{scatt}(\omega - \omega_0 - kv) - F_{scatt}(\omega - \omega_0 + kv), \tag{8}$$

and if we make an expansion of the force to consider only low velocities, i.e. $kv < \Gamma$ we get

$$\begin{aligned} F_{molasses} &\approx F_{scatt}(\omega - \omega_0) - kv\frac{\partial F}{\partial \omega} - \left[F_{scatt}(\omega - \omega_0) + kv\frac{\partial F}{\partial \omega}\right], \\ &\approx -2kv\frac{\partial F}{\partial \omega}, \\ &\approx -\alpha v, \end{aligned} \tag{9}$$

where $\alpha = 2k\frac{\partial F}{\partial \omega}$. This is a force similar to the one a particle experiences when it moves through a viscous fluid, therefore the name of the technique: optical molasses. In the actual experiment, it is important to use pairs of counter-propagating beams in all three directions to effectively slow down the atoms.

This is a very successful technique of cooling neutral atoms. If we take alkaline metals as example, the lower temperature achievable is of hundreds of μK [20], an outstanding result. This lower limit is imposed by spontaneous emission of the atoms. Once a photon of the cooling beam is absorbed, the atom must re-emit this photon in a random direction. To preserve momentum conservation, it must move in the opposite direction with a certain recoil velocity. By associating a temperature to this velocity, we find the Doppler cooling limit, which is the lower temperature we can achieve through the optical molasses technique.

An observant reader will notice that although the atoms may accumulate in the region of intersection of the beams, because of their tiny velocities, they are not actually trapped. Eventually, they will leave the interaction region and regain speed. To trap them, we must use

a specific type of polarization in the beams combined with a magnetic field gradient, as first suggested by Jean Dalibard [21].

In this scheme, called magneto-optical trap, we add to the experimental setup of the optical molasses a pair of coils in the anti-Helmholtz configuration, i.e. their currents have different directions. This pair of coils generates an uniform field gradient near the point in the middle of them. This means that the atoms will experience a Zeeman shift in their energy levels. This shift can be explored, along with the selection rules, to add a new term in the force of Eq. (9).

Let us look in detail how this field gradient and the lasers act together. For that, consider a simple transition $|F_g = 0\rangle \rightarrow |F_e = 1\rangle$ as shown in Fig. 4. The pair of counter-propagating beams have orthogonal and circular polarization, so they will only interact with the group of atoms that have the correct position regarding the center of the trap. This is caused by the selection rule of angular momentum. A σ^+ beam may only cause transitions that increases the angular momentum by one unity, while a σ^- polarization causes only transitions that decreases the angular momentum.

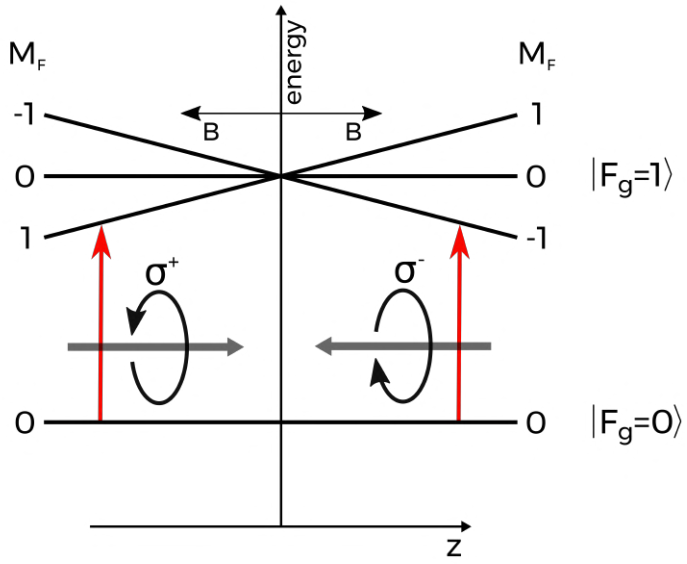

Figure 4 – Magneto-optical trap: counter-propagating lasers with circular polarization acting on a moving atom through a magnetic field gradient.

We might rewrite Eq. (8) if we consider the Zeeman effect in the detuning of the lasers, i.e. $\delta = \omega + kv - (\omega_0 - \beta z)$. The Zeeman shift is given by βz, where β depends on $\frac{dB}{dz}$. By doing the same previous expansion, we arrive at:

$$F_{MOT} \approx -\alpha v - \frac{\alpha\beta}{k} z. \tag{10}$$

There is a new term, a restoring force, meaning that the dynamics of the atoms in the trap follows a harmonic motion, typically over-damped [18]. A simplified scheme of the apparatus to trap the atoms is presented in Fig. 5.

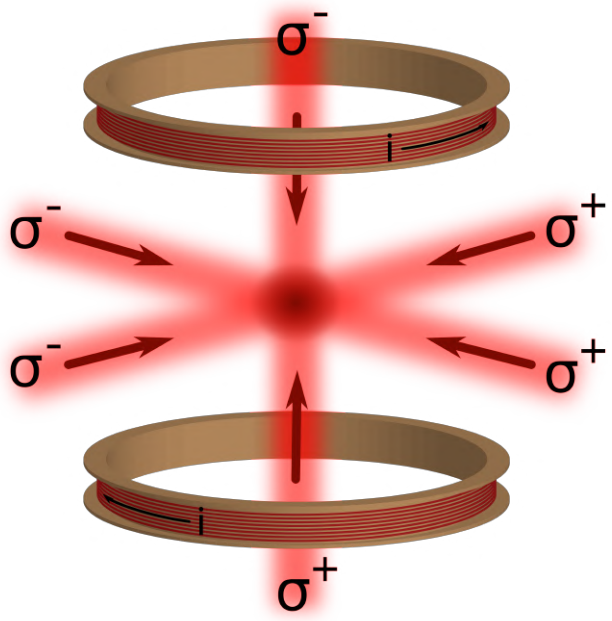

Figure 5 – Magneto-optical trap scheme.

Magneto-optical traps provide good sources of cold atoms for a wide range of experiments. It is an easy to load trap, with typical capture velocities of tens of *m/s* [22], and up to 10^{10} trapped atoms. Surely, these numbers may change a lot from a specific setup to another. We must also emphasize that this is not a magnetic trap. The field gradient in a MOT is much smaller than in pure magnetic traps (not even enough to hold the atoms against gravity), so that the forces in play are due to the lasers.

2 EXPERIMENT

In this chapter we describe the details of our experimental setup for the magneto-optical trap and the specific procedures to induce the FWM processes and measure the generated signals.

2.1 Experimental Setup

The cooled atoms must stay in a very low pressure environment to avoid collisions and consequently the loss of the trap. This implies that the experiment requires a good vacuum system. For the MOT, the often used type of pump is an ionic pump, in our case, a *Starcell* from Varian. This pump operates typically in an ultra-high vacuum regime, i.e. ~10^{-9} Torr. It ionizes the gas inside the chamber and accelerates these ions with a high electric potential, ranging from 3 kV to 7 kV. One of the main reasons for using ionic pumps in cold atoms experiments is that it does not have moving parts and no need of oil. Thus, they require little maintenance and produce almost no noise.

The vacuum pump is connected to a glass chamber, henceforth labeled *science chamber*, where the lasers can interact with the atoms. It is also in the science chamber that lies the rubidium dispenser. This dispenser contains a mixture of a rubidium compound and a reducing agent [23]. The alkali metal is released in a controllable way via ohmic heating, with currents typically from 5 A to 7 A and reaching temperatures up to ~800 ^{o}C.

The following aspect of the experiment is the magnetic field. We use a pair of circular coils with a radius of 27 mm and made of 1.1 mm diameter copper wire, rolled 50 times. As mentioned before, the coils are in an anti-Helmholtz configuration with a 1.5 A current, i.e. the currents go in different directions. The final arrangement is similar to the one presented in Fig. 5, with a typical gradient of magnetic field inside the science chamber of 10 G/cm.

In addition to this magnetic field there are also compensation coils that shield the atoms from external fields, specially the earth magnetic field. The cage is made of three pairs of square coils, arranged to form a cube, so that each pair can generate a field in a specific direction. The sum of these vectors can act against earth's magnetic field and eliminate it. For our system we coarsely tuned the currents in the cage, but a precise procedure can be used as shown in Ref. [24].

The main segment on the experiment is the optical setup. We use two diode lasers from *Sanyo*, model DL7140-201S with homemade electronics. These are reasonably narrow lasers, with linewidths below 1 MHz and the possibility to sweep the frequency over 10 GHz by changing the injection current. This range of frequency is more than enough to interact with all hyperfine levels of the D_2 line of ^{87}Rb (at 780 nm), shown in the level diagram of Fig. 6.

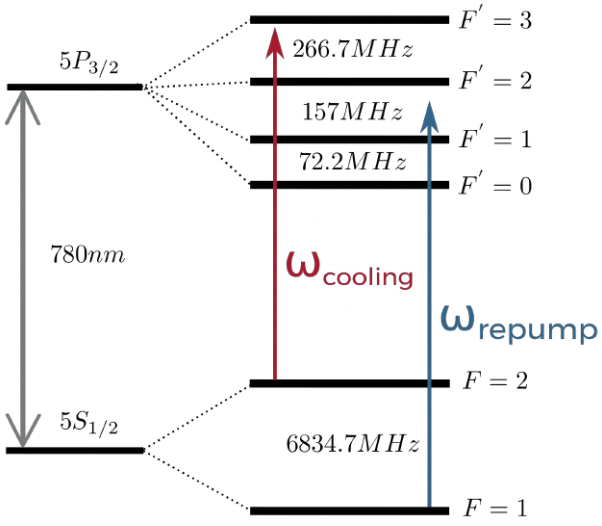

Figure 6 – Level diagram of the D_2 line of ^{87}Rb with the cooling and repump transitions in red and blue, respectively.

The two diode lasers are labeled cooling and repump. The cooling laser is the main responsible for the MOT mechanism, transferring momentum to the atoms via absorption. It is tuned near the transition $|F_g = 2\rangle \rightarrow |F'_e = 3\rangle$. Although this transition is closed, i.e. it only relaxes to its original ground state, some atoms may go to $|F'_e = 2\rangle$ due to the high intensity of the lasers and the Doppler broadening. Therefore, these atoms might fall in the $|F_g = 1\rangle$, where they can no longer interact with the cooling laser, i.e. a dark state. To deal with these atoms there is the repump laser tuned in the open transition $|F_g = 1\rangle \rightarrow |F'_e = 2\rangle$.

Each diode laser has their own reference cell, associated with a saturated absorption spectroscopy (SAS), shown in the simplified scheme of Fig. 7. Right after the laser, there is a 60 dB optical isolator from *Isowave*, to prevent reflected light of reaching the diode and causing any damage. Since only a small fraction of the laser power is necessary to perform the SAS, we use a microscope slide to divide the beam in two parts. The more intense beam goes to the MOT, while the weaker is used in the SAS.

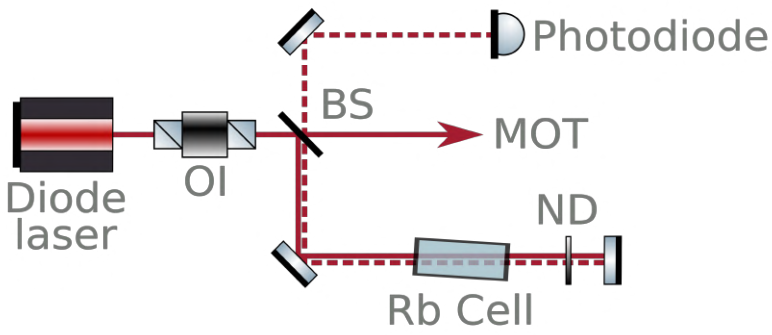

Figure 7 – Simplified scheme of the saturated absorption spectroscopy. OI, BS and ND are optical isolator, beam-splitter and neutral density filter, respectively.

The SAS technique, a well known type of Doppler-free spectroscopy, uses a pair of counter-propagating beams to distinguish the hyperfine levels of an atomic vapor. These beams are called pump and probe, the later being less intense, and they interact, in our system, with a sample of rubidium. Our vapor cells contain both stable isotopes of rubidium in natural abundance, i.e. 72.2% of ^{85}Rb and 27.8% of ^{87}Rb.

The pump and probe beams are broadly absorbed by the medium due to the Doppler effect. However, when both lasers have the correct frequency of one the hyperfine levels and interact with the same velocity group of atoms, the probe beam is less absorbed resulting in a peak in the transmission measurement, as shown in Fig. 8. Notice that there are four absorption dips in this result because each isotope has two hyperfine ground states (see Fig. 6). Inside each one of these dips there are six peaks, meaning that in six occasions the pump and probe beams were interacting with the same atoms.

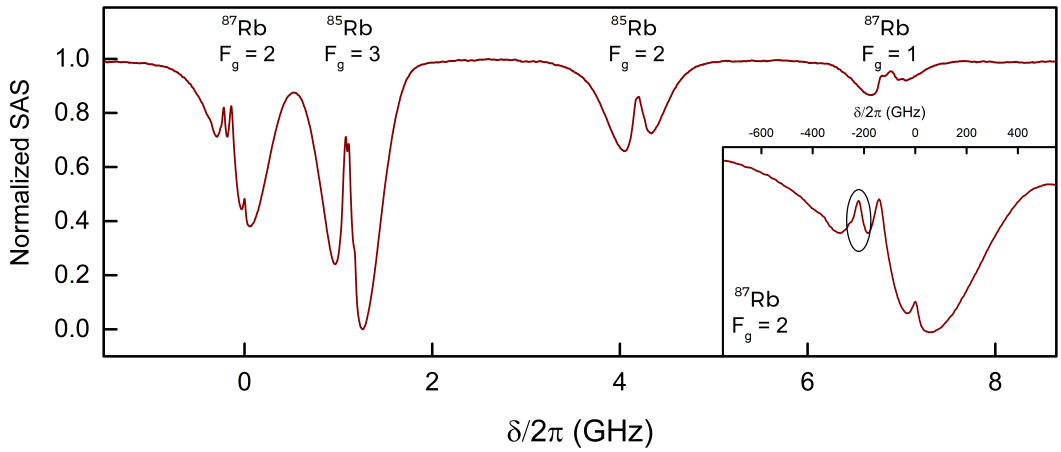

Figure 8 – Saturated absorption spectroscopy of the Rb. The zero of the horizontal axis corresponds to the closed transition $|F_g = 2\rangle \rightarrow |F'_e = 3\rangle$ of ^{87}Rb. The inset graph is a zoom of this last transition with the crossover between $|F'_e = 1\rangle$ and $|F'_e = 3\rangle$ circled.

Due to angular momentum selection rules, only three transitions are allowed from the hyperfine ground states. Thus, only in three out of these six peaks both beams are interacting with the same hyperfine level. The other three peaks are crossover transitions, i.e. the pump beam is resonant with one hyperfine while the probe interacts with a different one, for the same group of atoms.

At all times during the operation of the MOT we use the SAS signal to keep track of the frequency of both lasers, cooling and repump. To properly trap the atoms, the cooling laser is actually in the crossover between $|F'_e = 1\rangle$ and $|F'_e = 3\rangle$. To bring its frequency near the closed transition we use an acoustic-optical modulator (AOM), leaving a small detuning from the $|F'_e = 3\rangle$ level. This is important to interact with a greater number of atoms, because if the laser frequency is set completely in resonance only the stationary group of atoms will be able to interact with it.

The beams not used in the SAS, are applied in the actual assembly of the MOT. A simplified scheme of the MOT lasers and the combination for the three arms X, Y and Z is presented in Fig. 9. The repump laser goes directly to a fused fiber optic coupler, i.e. a cable in X-shape that has two inputs and two outputs. As shown in the scheme, the inputs are the repump and cooling beams. The outputs are the *X* and *Y* arms of the trap.

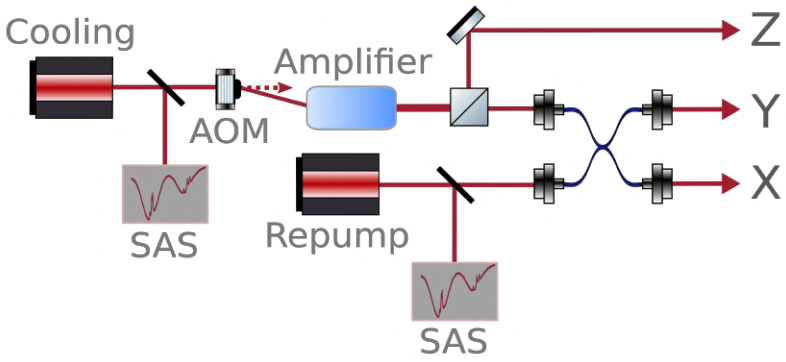

Figure 9 – Simplified setup of the MOT lasers. SAS and AOM are saturated absorption spectroscopy and acoustic-optical modulator, respectively.

Before arriving at the fused fiber optic coupler, the cooling laser has several steps. After the SAS, it needs to go through an AOM. This happens for two reasons. The first is that we use this AOM to modulate the cooling laser in order to switch the MOT in a controlled temporal scheme. This temporal control is explained in the next section. Secondly, the cooling laser must have a small detuning to optimally cool the atoms. In this case the chosen crossover transition to fix the laser frequency is 212 MHz below the $|F_e = 3\rangle$ level. The AOM blue shifts the laser frequency by 200 MHz for the first order, leaving it only 12 MHz from the cyclic transition. We also use the zero order of the AOM, indicated by the dotted arrow in Fig. 9, in other parts of the experiment, e.g. as a guide beam for alignments or to measure the optical density of the MOT.

Since there are many optical elements in the path of the cooling beam before arriving at the atoms, a lot of power is lost. Our diode lasers have typical powers of tens of mW, making necessary the use of an amplifier to compensate the losses. We use a *Boosta* amplifier from *Toptica Photonics*. In an optimal alignment situation, an input power of 20 mW becomes an output power of 700 mW. With such gain, there is enough power to generate all arms of the MOT.

The output light of the amplifier is coupled to a fiber and sent to its final step before the fused fiber optic coupler. In this part, we use a polarizing beam-splitter (PBS) to separate two beams. One of them is sent directly to the *Z* arm of the trap, while the other is sent to the fused fiber optic coupler to be mixed with the repump. With all three beams ready, they are sent through fibers to the science chamber. Once out of a fiber, a telescope is used to expand these beams to a 5 cm diameter and a quarter-wave plate changes their linear polarization to

the proper circular polarization. Once the laser passes through the chamber, a mirror reflects it back, forming the pair of counter-propagating lasers as indicated in the picture of the system in Fig. 10. These reflected beams double-pass through a quarter-wave plate to acquire the correct orthogonal polarization.

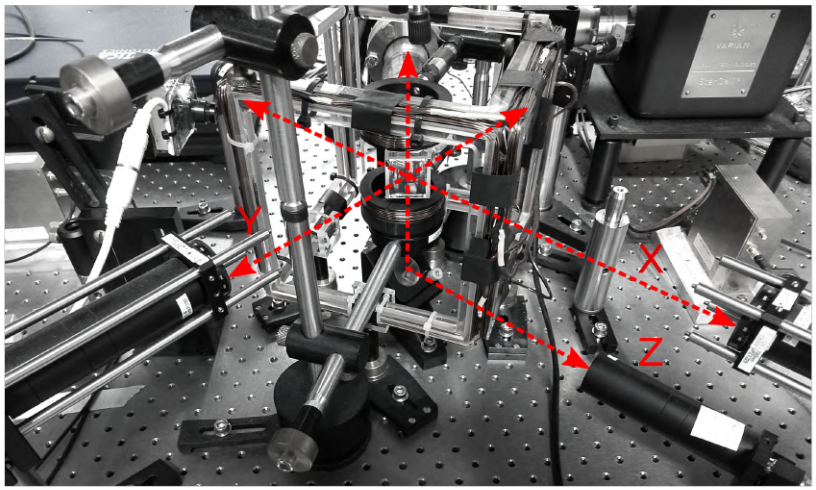

Figure 10 – Picture of the science chamber with the MOT arms indicated by the red dashed lines.

The MOT itself is observed with an IR camera, since the light used in the trap process is emitted via spontaneous emission in all directions. It is also possible to capture an image of the trapped atoms using a CCD camera. These images are useful to measure the diameter of the cloud, as shown in Fig. 11, by transforming the picture into a matrix with the individual information of each pixel. Then we plot the data of the sum of rows or the sum of columns and fit them with a Gaussian. We use the waist of this Gaussian as the diameter of the MOT. In fact, the cloud is slightly elliptical and therefore we measure the horizontal and vertical profiles. The result in Fig. 11 is within the usual parameters of our system, with a 4 mm diameter.

The same fluorescence that allows the CCD to capture images of the cloud might be used to measure the number of atoms. In this case we use a photodetector (DET36 from *Thorlabs*) that captures this fluorescence with the aid of a lens. Using the peak response of the photodetector we may calculate the total power detected in that solid angle. By generalizing to a sphere, we know the total power emitted by the atoms. Finally, we divide this total power by the energy of a single photon and the scattering rate, finding the number of atoms. For our experimental setup, this number typically has the order of 10^9 atoms.

The MOT diameter and number of atoms are a fraction of the several parameters that can be obtained from characterization measurements [25]. One last parameter that we measure is the optical depth (OD), a number that represents how much light the MOT can absorb. For this, we use a attenuated beam on resonance with the closed transition $\left|F_g = 2\right\rangle \rightarrow \left|F'_e = 3\right\rangle$ and acquire its transmitted intensity with the MOT on (I) and off (I_0). Then, the optical depth is

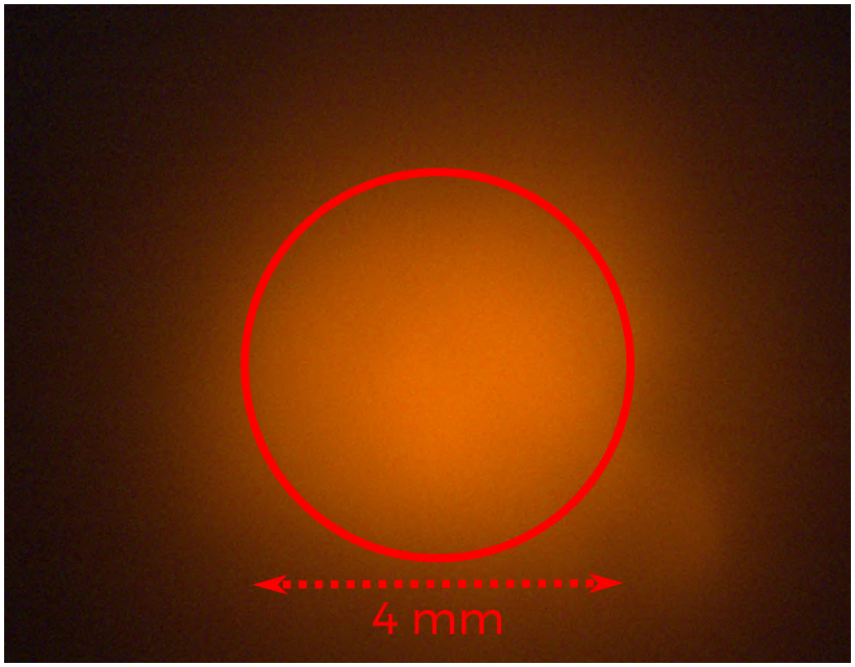

Figure 11 – CCD image of the atomic cloud. The red line indicates the diameter taken from the Gaussian fit.

simply $OD = -Ln(I/I_0)$, with the typical values of our system ranging from $OD = 3$ to $OD = 4$.

2.2 Four-Wave Mixing Setup

As mentioned previously, the initial goal of this work was to analyze two signals of FWM generated with the same atomic sample and only one laser. To do so we have mounted the setup presented in Fig. 12, where a single *cw* laser generates two linear and orthogonal polarized beams, labeled input beams a and b. This *cw* laser is similar to the cooling and repump lasers of the MOT and therefore can be tuned by directly changing the injection current. It is worth mentioning that for the FWM part of the experimental setup there is also a SAS experiment right after the *cw* laser, just as it is in the MOT.

In a typical configuration of FWM, we would have a strong beam with a fixed frequency and a weaker beam that probes the system while scanning its frequency. In our case, both beams have almost the same intensity and we are interested in the two FWM signals generated in directions $2\vec{k}_a - \vec{k}_b$ and $2\vec{k}_b - \vec{k}_a$, as shown in Fig. 13. This means that we are investigating processes where two photons of one of the beams are absorbed and one photon of the other beam is emitted, generating new coherent signals. In addition, we can only scan the frequency of the laser itself, meaning that both beams have their frequencies changing simultaneously. The input beams also have a small angle of 10 mrad to allow to spatially separate all four signals. This configuration leads to FWM spectra with unexpected features. These features are the main objective of this work.

The two FWM signals and the transmissions of the input beams a and b are detected by

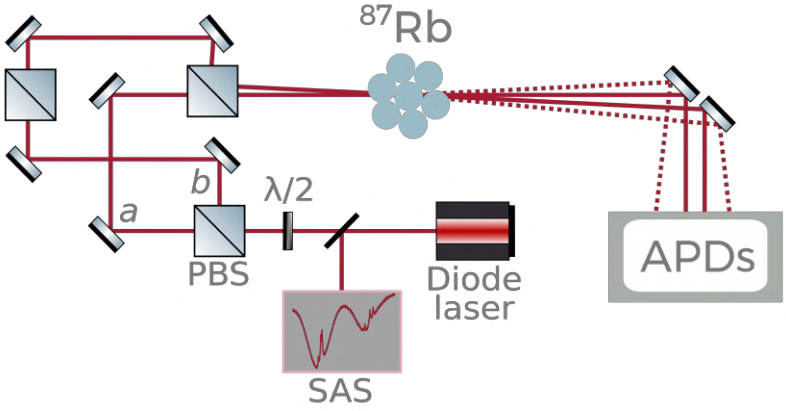

Figure 12 – Simplified scheme of the four-wave mixing setup. PBS and APD are polarizing beam-splitter and avalanche photodiode, respectively.

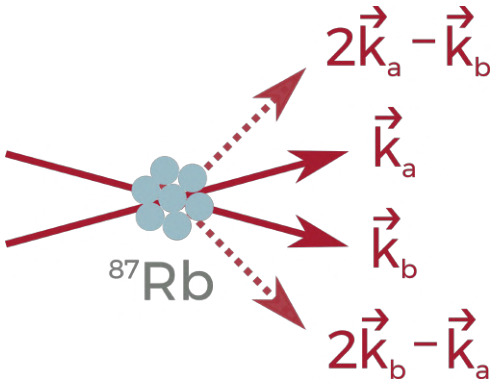

Figure 13 – Spatial distribution of the input beams and FWM signals.

avalanche photodiodes (APD) of the models APD120A/M (max responsivity at 800 nm) and APD120A2/M (max responsivity at 600 nm) from *Thorlabs*, respectively. We use these detectors because they are highly sensitive and for our experimental situation the FWM light can be fairly small. To achieve this great sensitivity, APDs provide gain in the input signal via the process of avalanche multiplication.

The beams that induce the FWM processes are tuned near the closed transition $|F_g = 2\rangle \rightarrow |F'_e = 3\rangle$, where it is reasonable to expect the greatest signal. Since this is the same transition of the cooling laser of the MOT, both lasers might compete for the atoms, making the FWM process inefficient. To avoid this, we use a temporal scheme to generate and acquire the signal of interest with the MOT lasers off. In our case, we built a time control apparatus using an *Arduino* board that temporally manages the entire experiment. Fig. 14 shows a scheme of this temporal control.

All trapping fields, i.e. cooling laser and anti-Helmholtz (AH) coil, are shut down in a 2 ms window. This time is small enough so that the atoms cannot gain much speed and therefore move away of the center of the science chamber. It is in this window that we obtain the whole FWM signal. The trigger (red curve in Fig. 14) has a small delay of 20 μs, allowing the repump

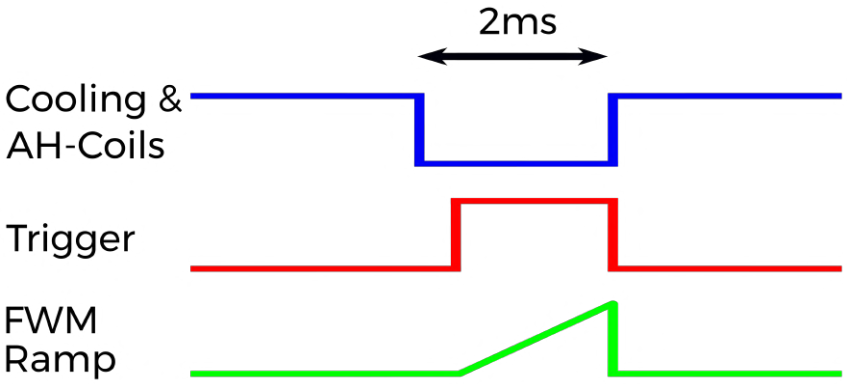

Figure 14 – Temporal control of the FWM experiment.

laser to properly prepare the atoms in the ground state $\left|F_g = 2\right\rangle$, where they can interact with the FWM laser. In fact the repump laser is always active throughout the measurement. This trigger controls a ramp that modulates the injection current of the FWM laser, scanning the frequency of beams a and b (green curve in Fig. 14).

This time control scheme is often used in experiments with cold atoms. It is typically coupled with a data acquisition system that shifts the laser detuning by small amounts from one time window to the next. This way, the system acquires one point of data per window. We actually have designed and tested in the past an acquisition system based on *LabView*. However, for the experiment described here, such a system is not reliable because our MOT lasers do not have their frequencies locked. As a consequence, our sample is unstable due to the drift in frequency of the cooling and repump lasers. Without the frequency locking system, the atomic cloud stays in place for only a few minutes, while with the locking it could stay for hours.

Given that, we perform the whole FWM measurement in a single time window. In terms of numerical parameters, this means a 250 Hz ramp whereas the amplitude depends on the intensity of the input beams. This intensity dependency comes from the spatial configuration where both beams are copropagating and therefore are pushing the atoms with the same force that holds them in the center of the cell. This radiation pressure is higher on resonance, so we cannot scan the FWM laser slowly, otherwise the atoms will gain too much velocity and leave the trap. One alternative to actually leave one of the beams fixed on resonance would be to use an AOM to produce small pulses ($\sim \mu$s). This way there would not be enough energy to push the atoms away. However, we do not have an AOM available to do this, so the only option is to use fast scans.

Therefore, to choose the amplitude of the ramp it must be big enough so that the lasers are not resonant for too much time and push the atoms away. For a configuration where the intensities are $I_a = I_b = 10$ mW/cm^2 we have used typically 3 V ramps. This gives a frequency range great enough to see all three hyperfine transitions, which can be used to extract a time-frequency conversion factor. In Fig. 15 we present a typical measurement of the transmission of beams a and b that we use to extract this conversion factor.

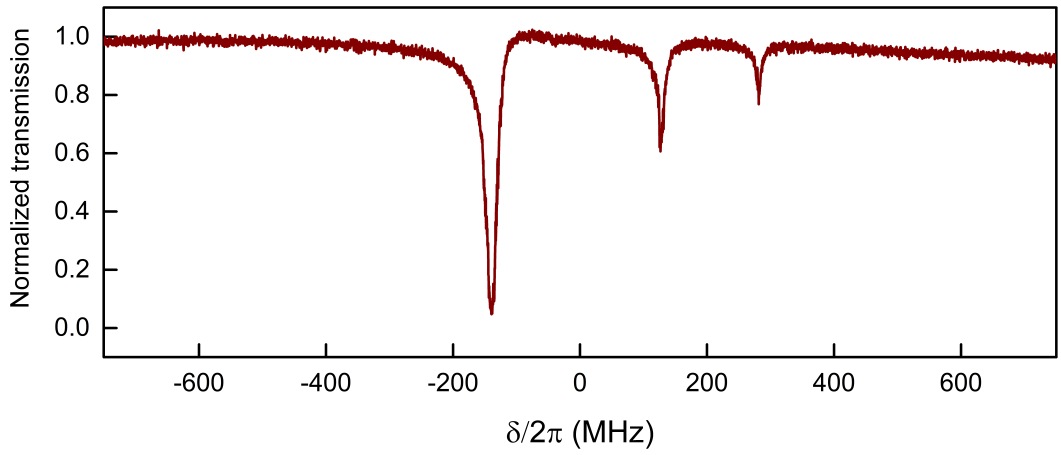

Figure 15 – Transmission of a weak beam through the cold atoms as a function of the detuning.

With the conversion factor in hand we can estimate how long the laser stays on resonance. For a 3 V amplitude it takes 2.5 μs to shift 1 MHz and since the natural linewidth is about 6 MHz [26], we may say that the lasers stay 15 μs on resonance. With this information, we may also check for another phenomenon: even if the lasers are not strong enough to push the atoms away, they may give enough velocity to an atom so that the Doppler effect takes it out of resonance.

To check this hypothesis, we begin by saying that the necessary Doppler shift should be equal to the natural linewidth (Γ) of the transition, i.e.

$$kv = \Gamma, \tag{11}$$

where k is the wavevector and v is the velocity of the atoms. This velocity comes from the momentum given by the photons, so, using momentum conservation

$$n\hbar k = mv, \tag{12}$$

where n is the number of photons and m the mass of the ^{87}Rb. Putting these two equations together we get

$$n = \frac{m\Gamma}{\hbar k^2}. \tag{13}$$

Using the known values we arrive at $n \approx 10^3$ photons for a single atom. Therefore, with the typical 10^9 atoms in the MOT, measured with the fluorescence, we would need 10^{12} photons to shift them away of resonance. In the 15 μs of our estimation, the 10 mW/cm^2 with a 1.5 mm diameter, laser gives only $\sim 10^{10}$ photons, at least two orders below the necessary amount. So, in our measurements we are safely far from pushing the atoms out of resonance and out of the trap.

3 EXPERIMENTAL RESULTS

In this chapter we describe a series of experimental results as well as the related discussions. For each parameter changed in the experiment there is a specific section presenting the results.

3.1 Two lasers measurements

Most of the performed measurements were done with a single laser setup, as previously described. However, there were a few initial attempts with two independent lasers. These measurements are necessarily more difficult since both lasers have to be simultaneously on resonance with the atoms in order to induce the FWM process. This is not an easy task without an AOM and a frequency locking system, therefore, we only made a few series of measurements using this configuration. The setup is similar to that described before, only that now the beams *a* and *b* are coming from two different lasers. A typical spectrum is presented in Fig. 16.

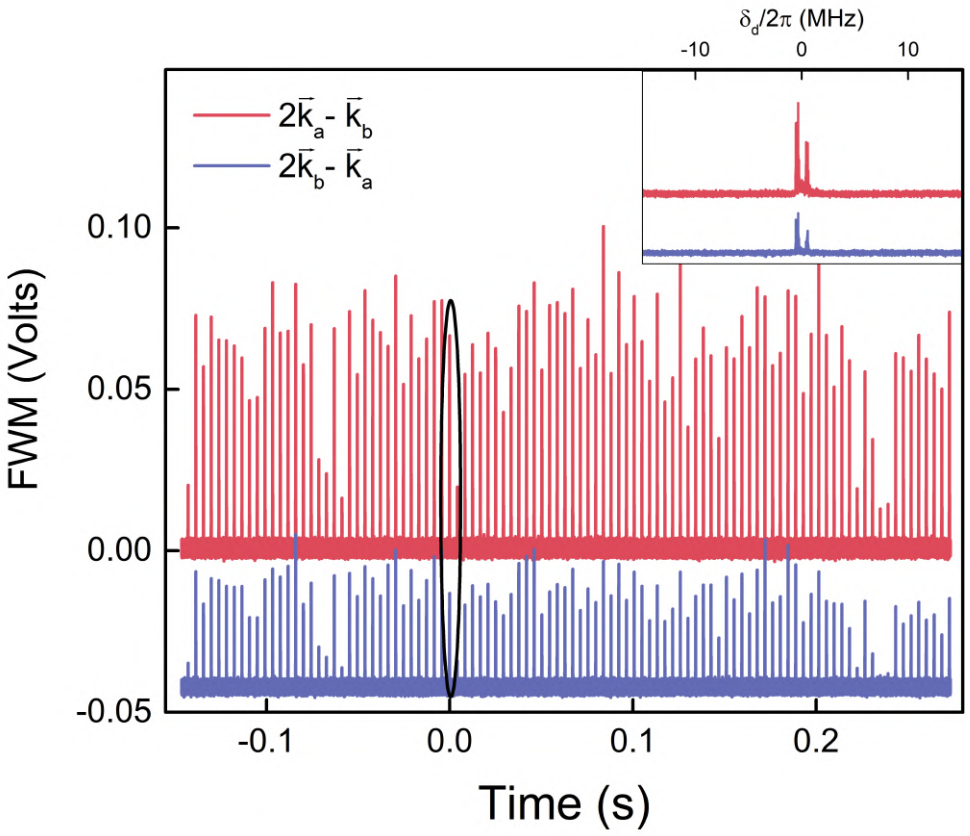

Figure 16 – Two hundred FWM spectra using two different lasers both with I $\approx$ 1 mW/cm^2. One of the signals was vertically shifted to improve visualization. The inset represents a zoom of the circled area.

Since there was little control of the lasers frequency, we took large scans containing

several time windows with FWM signals. For this particular result in Fig. 16 there are 100 of each FWM process, $2\vec{k}_a - \vec{k}_b$ and $2\vec{k}_b - \vec{k}_a$, taken with 10^7 Samples/s and a ramp frequency and amplitude of 250 Hz and 500 mV, respectively. The idea behind this type of measurement is to let all the lasers drift (the two needed for the FWM processes and the other two of the MOT) so everything that could happen would be recorded.

It is important to emphasize that, although the APDs used to detect this signal are very sensitive, the signal is never greater than 100 mV in this setup. This weak response is probably due to the input beams not being perfectly resonant with the atoms at the same time. It is hard then to analyze in detail the zoom curve in the inset graph of Fig. 16. It is only possible to say that the signal is quite narrow and appears to have some doublet structure.

To analyze all signals acquired, a huge amount of data ranging from 100 to 5000 windows, we wrote a *Python* code. The code would essentially locate all the peaks and store information about their position and amplitude. With these information we were able to perform a series of analyses of which only a few rendered understandable results. Three of those are shown in Fig. 17. The conclusions taken from these analyses are not encouraging. From the amplitude analysis (Fig. 17 (a)) we see that the FWM signals behave similarly with respect to this parameter, i.e. if one them increases so does the other. The factor of 2 between the signals comes simply from the fact that the $2\vec{k}_b - \vec{k}_a$ signal is detected a meter after $2\vec{k}_a - \vec{k}_b$, so it has a larger distance to defocus.

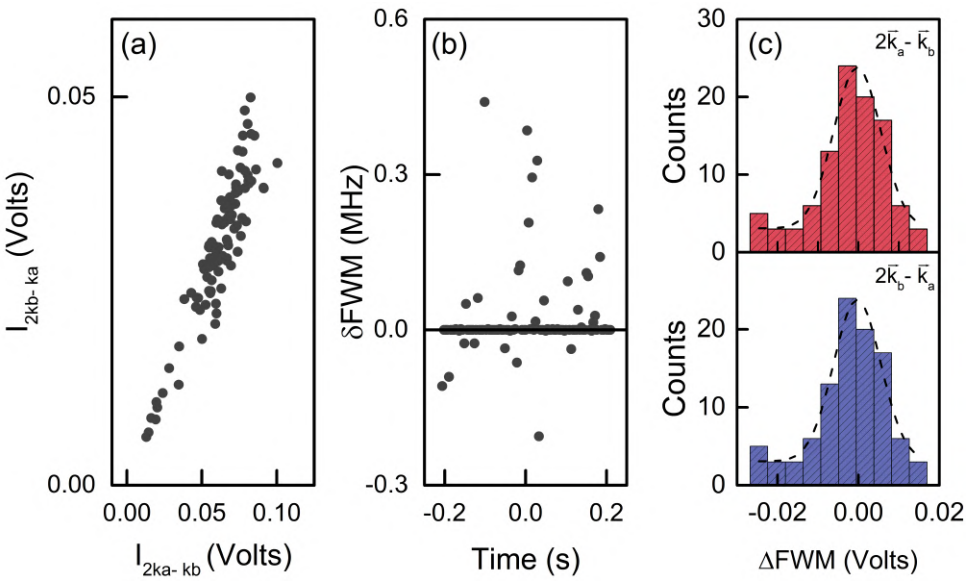

Figure 17 – (a) Amplitude of one FWM signal as a function of the other amplitude. (b) Detuning between FWM signals (δFWM) as a function of the detection time. (c) Histograms of the FWM amplitude, with respect to the average amplitude (ΔFWM).

Since the two lasers are not perfectly on resonance, the FWM signals should have some detuning between them. To measure this detuning is to look at the delay between the peaks of the FWM signals. This delays translates into a frequency difference, represented in the vertical

axis of Fig. 17 (b). For this particular measurement, this difference is in the range of 0.5 MHz, while for other measurements with more detection windows this range may go up to 2 MHz. This means that the FWM process can only be induced if the detuning between the input beams is in this narrow range of few MHz. This is a reasonable result because it is not expected that the cold atoms can interact with a laser too far from resonance.

Finally, the two histograms presented in Fig. 17 (c) represent the counting of the amplitude of the signals, with the center being the average amplitude. A Gaussian fits the data with a coefficient of determination $R^2 \approx 96\%$, meaning that the FWM signal is following a normal distribution. Hence, the fluctuations of the FWM signal amplitude must be only due to the lasers frequency drift, a process that is not controlled.

Nonetheless, there is an apparent correlation between the signals $2\vec{k}_a - \vec{k}_b$ and $2\vec{k}_b - \vec{k}_a$, i.e. they present similar behaviors. To quantify such correlation we have measured the Pearson coefficient [27] between the two signals and found a 91% positive correlation. This coefficient measures if there is statistical evidence of a linear relation between two given variables. Therefore, it confirms that the FWM signals do present a strong correlation. We must emphasize that this correlation should have a classical nature, since each signal must be generated by different atoms for a given time.

These measurements are time consuming, since we must keep track of four unlocked lasers manually. One reasonable way of making this simpler is using a single cw laser to generate the two FWM input beams. Thus, in the following sections we will only discuss measurements performed with this simpler setup.

3.2 Intensity

With the single laser setup the FWM spectra is a lot more easier to obtain and robust. It opens the possibility then, to change specific parameters of the system and carefully analyze the spectra. However, before getting into this detailed analysis it is important to look at a typical result, such as the one presented in Fig. 18.

This experimental result is one of many taken throughout this work and it represents well the typical outcome for the single laser setup. The curves in Fig. 18 (a) are the transmissions of the input beams. They are slightly asymmetric, possibly due to the scanning direction as will be discussed in the last section of this chapter. For this and all following results the scanning direction went from high energies to low energies and are inverted in the presented graphs to match the frequency direction, i.e. high frequency means high energy. As for the parameters for the frequency scan of the cw laser, they are also the same for all experimental results, except when mentioned, with a 250 Hz frequency and 3 V amplitude ramp.

The main object of this study is presented in Fig. 18 (b) with the FWM signal detected. Two features draw attention, the similarity between the two signals and the deep valley around

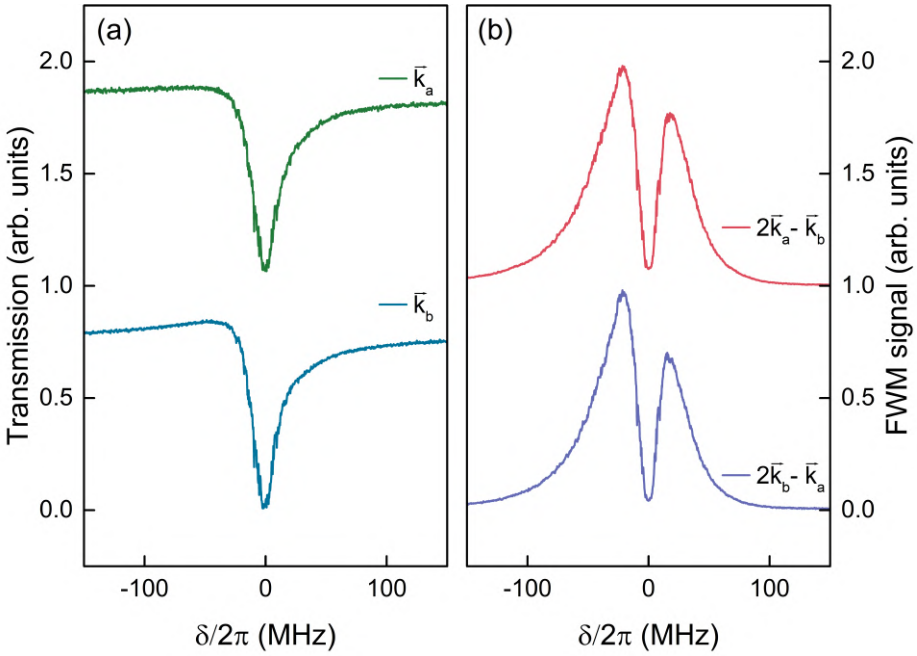

Figure 18 – (a) Transmission of the input beams both with I ≈ 10 mW/cm^2. (b) FWM spectra using a single laser. All curves are normalized.

the resonance. The first one was already expected given the high positive correlation between signals as demonstrated previously with the two lasers setup. Also the two signals are generated through the same type of FWM process, using the same beams, both with same intensities. So, they should be identical. However, the second feature, the valley, was unexpected.

One might say that a valley such as this should only be due to absorption effects, since we are dealing with a highly absorbing media. Another possibility would be an Autler-Townes splitting [28, 29] caused by the lasers given that they are, for this particular result, a few times above saturation intensity. If that was case, the lasers would split the levels of the transition in two, leading to more than one possible excitation routes of the FWM process. To check this first two hypothesis we performed measurements changing the intensity of the input beams, as presented in Fig. 19.

Let us start the analyses by Fig. 19 (a). These three spectra were taken using different intensities of both input beams, with the curves normalized to allow a superposition. Clearly there is a power broadening effect in this result, considering that the higher intensity curves have a larger width. Despite that, the valley remains with nearly the same width. In fact, we changed the intensity of the input beams in a range of two orders below to two orders above saturation intensity and the valley remained with the same shape. It becomes clear then that the Autler-Townes hypothesis must be ruled out, because there should be no splitting below saturation intensity and for high intensities there should be two well separated peaks.

At this point another hypothesis to explain the valley that can be ruled out is the electromagnetically induced absorption (EIA) [30]. In this phenomenon there is large increase in

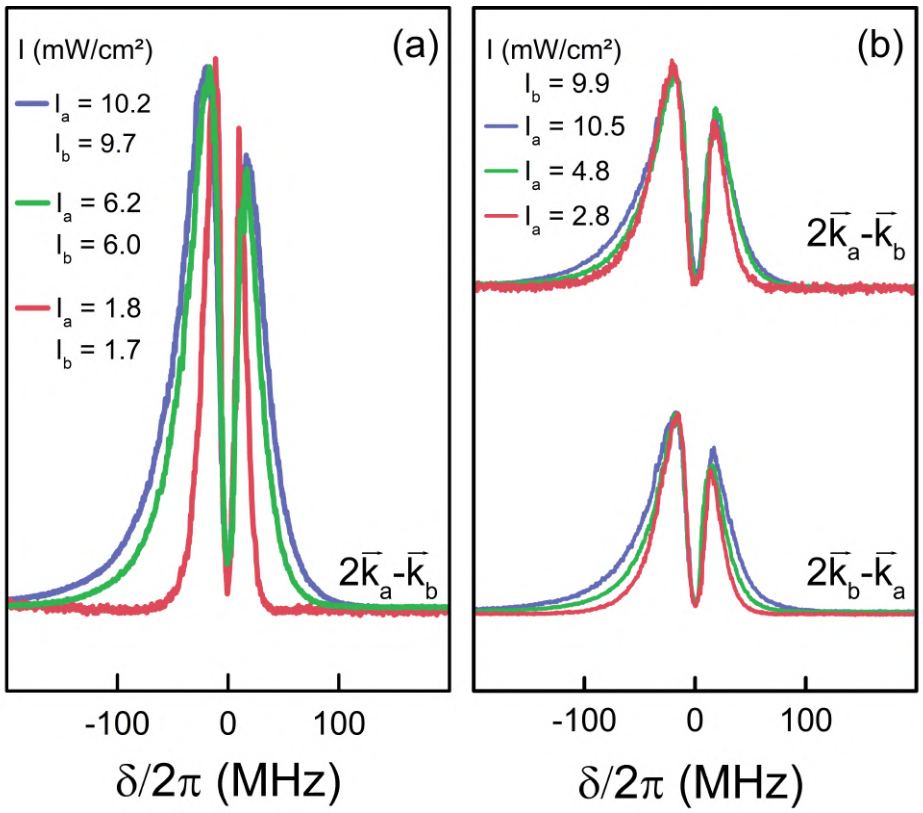

Figure 19 – (a) FWM spectra for different intensities of both input beams. (b) FWM spectra for different intensities of a single input beam. All curves are normalized.

atomic absorption due to the interaction with resonant light. Since the sublevel structure of our experiment matches the necessary conditions for EIA, it could explain the valley in the FWM signal. However, the literature [31] shows that the increase in absorption due to EIA is very narrow in frequency, i.e. below the natural linewidth, and intensity dependent. Our signal violates these two conditions, so EIA must not play a role in this experiment.

To better understand the power broadening, we also changed the intensity of a single input beam to keep track of its effects in each FWM signal, as shown in Fig. 19 (b). In this case, the power broadening effect is less pronounced, specially in the upper curves that represent the signal $2\vec{k}_a$ - $\vec{k}_b$. One might expect that this signal, which depends on the absorption of two photons of the input beam $\vec{k}_a$, would be more affected by intensity changes of this same beam, but the results show otherwise.

Using the same techniques described in the previous section, i.e. acquire large quantities of data and extracting information with a *Python* code, we were able to analyze quantitatively a few features. These results, as a function of the total laser intensity $I = I_a + I_b$ and for the $2\vec{k}_a$ - $\vec{k}_b$ signal, are given in Fig. 20.

On Fig. 20 (a) we show that the amplitude of FWM signal grows with the intensity, without showing signs of saturation for the presented range. A linear fit of the data on a log-log graph shows that the exponent of this growth is ≈ 1.5. If we had changed the intensity of only

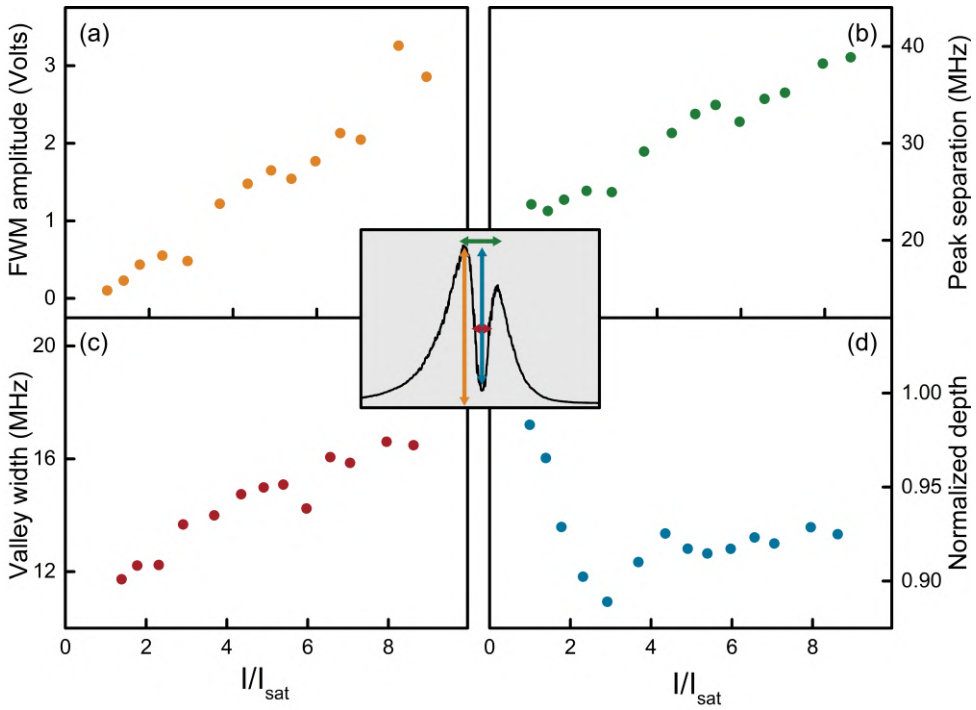

Figure 20 – (a) Amplitude of the FWM signal measured at the higher peak. (b) Frequency separation between FWM peaks. (c) Full width at half maximum of the valley. (d) Normalized depth of the valley, i.e. depth/amplitude. I_{sat} = 2.5 mW/cm^2 is the saturation intensity of the D_2 line of ^{87}Rb [26]. The experimental data comes from the $2\vec{k}_a$ - $\vec{k}_b$ signal. The arrows in the inset indicate each parameter measured by matching their colors.

the input beam *a*, the one that gives two photons to the FWM process, it would be expected that the FWM signal amplitude would have a second-order dependency on the laser intensity. On the other hand, changing only the intensity of the input beam *b* should induce a linear dependency of the FWM amplitude, since it contributes with one photon to the FWM process. Therefore, changing the total intensity should result in a third-order dependency, whilst we obtained an exponent of 1.5. This discrepancy is yet to understood.

As for the peak separation and the valley width, Fig. 20 (b) and (c) respectively, they appear to be connected. It is so because the FWM spectrum broadens with the increase of the intensity, as shown in Fig. 19 (a). However, the peak separation almost doubles for the intensity range of the graph, while the valley width increases only by a third. Thus, the whole signal width is more sensitive to intensity variations then the valley width.

The fourth result, in Fig. 20 (d) might give some insight on this odd discrepancy between the valley width and the peak separation. In this graph we present the normalized valley depth, i.e. the depth of the valley divided by the amplitude of the signal. Therefore, if this parameter decreases it means that the valley has become shallower and, in fact, this happens around the region where both lasers have their intensities equal to the saturation intensity. This small change of behavior of the valley depth around the saturation intensity indicates that there are different

physical phenomena acting on a low intensity regime and on a high intensity regime. It also may explain why the valley width (Fig. 20 (c)) seems to be less sensitive, i.e. only for higher intensities it would grow faster.

With all this data in hand, it is hard to support the idea of the valley being a mere absorption. Had this been the case, we would expect to see the valley depth decrease as the intensity increases. Therefore, absorption might only explain the valley depth until the saturation intensity. After this value, some other mechanism must play a role.

3.3 Optical depth

To further investigate the absorption hypothesis it is important to study the behavior of the FWM signal under different optical depths (OD). It is reasonable to expect that, if the valley is due to absorption, a sample with lower OD would absorb less and consequently produce a shallower valley. The experimental results are shown in Fig. 21.

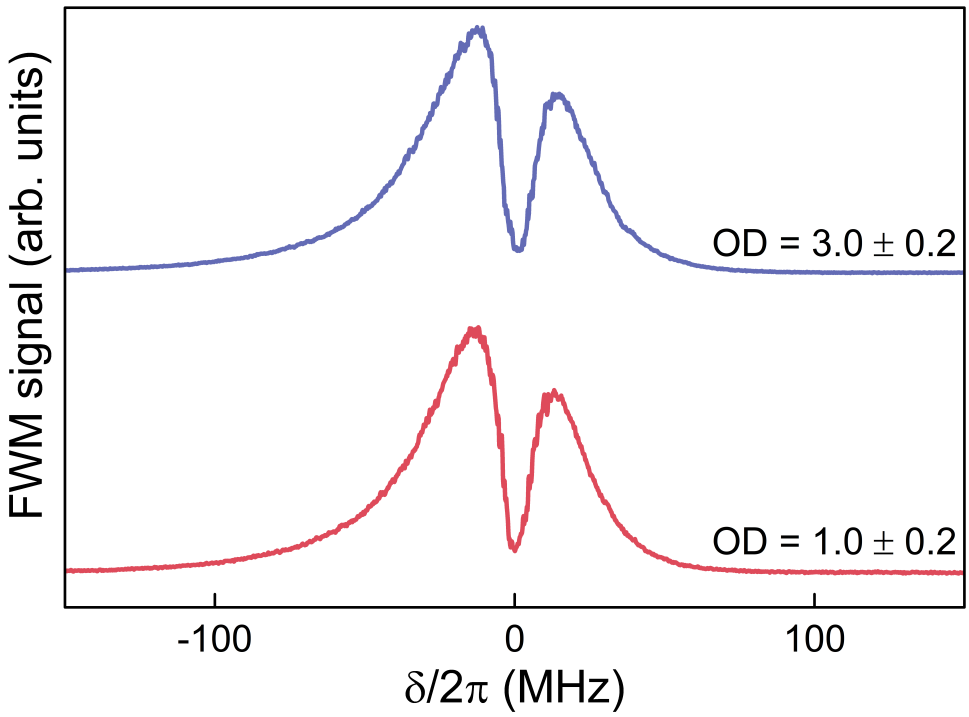

Figure 21 – FWM spectra for two regimes of optical depth. Input beams both with I ≈ 5 mW/cm^2. All curves are normalized and the data comes from the $2\vec{k}_a$ - $\vec{k}_b$ signal.

In order to change the OD of the MOT we used neutral density filters to lower the power of the cooling beams. By doing so, we could go from OD = 3 to a lower density regime with OD = 1. These values mean that for a weakened beam the sample went from a 95% to a 63% absorption. Our maximum value of OD is not as big as it should be, considering the values of the literature, but it is reasonable given the fact that the cooling and repump lasers do not have their frequencies locked.

The result in Fig. 21 shows that even though there are considerably less atoms to participate in FWM process and therefore to absorb the signal, the valley does not change. This is a strong evidence that some other effect must also play a role to explain the nature of this spectrum.

3.4 Circular polarization

Most of the measurements of this work were performed using linear and orthogonal polarized beams, as described in the previous chapter. However, it is interesting to ask how different the spectrum would be for circular and orthogonal polarized beams. These results are shown in Fig. 22. To perform such measurements, we have used a quarter-wave plate to transform the linear polarization into a circular one.

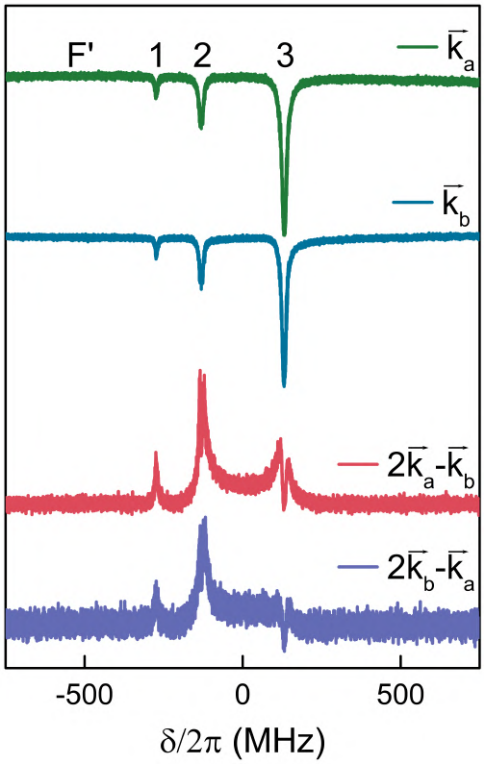

Figure 22 – Transmission of the input beams and FWM spectra using circular orthogonal polarization.

In this case we chose to present the transmission of the two beams over the FWM spectra to show the other two hyperfine transitions that the input beams may be resonant with, $|F_e' = 1\rangle$ and $|F_e' = 2\rangle$. The first aspect of this figure to draw attention to, is that the signal obtained in the closed transition $\left|F_g = 2\right\rangle \rightarrow |F_e' = 3\rangle$ becomes the two orders smaller than in the previous measurements with linear polarization. In fact, it is so small that the FWM in the open transition $\left|F_g = 2\right\rangle \rightarrow |F_e' = 2\rangle$ is larger.

To understand why this signal is so much smaller let us look in detail the Zeeman sublevels of this closed transition $\left|F_g = 2\right\rangle \rightarrow |F_e' = 3\rangle$. Fig. 23 has the possible transitions using

(a) linear and orthogonal polarization and (c) circular and orthogonal polarization. For linear polarization we might choose the quantization axis of the system as the polarization direction of one of the beams. Therefore, because of selection rules, this beam is only allowed to do π transitions while the other, which has two circular components (that together add up to a linear polarization), induces σ transitions (see Fig. 23 (a)). It is important to note that even though both lasers have linear polarization they cannot simultaneously connect the same states. As a consequence of that, the FWM signal may be generated in the basic four-level system of Fig. 23 (b). Several of these four-level systems may happen simultaneously and add up to the final signal.

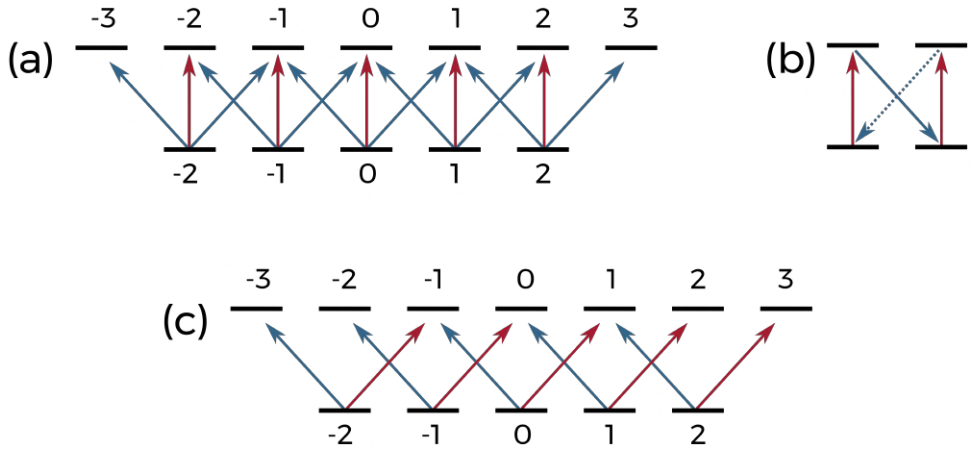

Figure 23 – (a) Zeeman sublevels of $\left|F_g = 2\right\rangle \rightarrow |F'_e = 3\rangle$ and the allowed transitions for linear and orthogonal polarized beams. (b) Unitary cell for the FWM in the linear configuration. (c) Zeeman sublevels of $\left|F_g = 2\right\rangle \rightarrow |F'_e = 3\rangle$ and the allowed transitions for circular and orthogonal polarized beams.

On the other hand, for a circular polarization setup both beams will induce σ transitions, one to greater m_F and the other to lower m_F (see Fig. 23 (c)). In this situation there is no possible arrangement to generate FWM, since the beams cannot complete the three necessary excitations. In addition, in the presented experimental result both lasers had the same intensity, so they should spread population evenly throughout all the ground sublevels. Therefore, the small FWM signal in Fig. 20 is due to the linear polarization residue, left in the beams by the quarter-wave plate.

3.5 Magnetic field

Considering the role of the Zeeman sublevels in the FWM process, the addition of a external magnetic field should have some impact on the spectrum. With the intent of testing this affirmation we have used the compensation coils of the MOT to increase the magnetic field perpendicular to the plane where the input beams and the FWM signal were. The spectra for different intensities of the external field are presented in Fig. 24.

Once again, all this curves are normalized to ease the comparison. It is clear that, up until 3 G, the magnetic field had no effect on the spectrum. This is actually reasonable since the closed

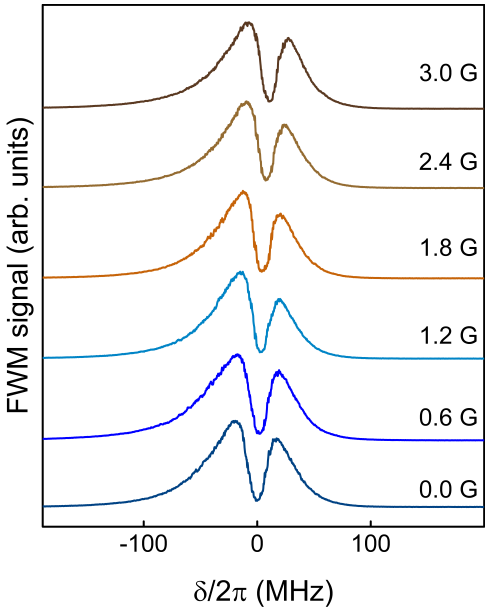

Figure 24 – FWM spectra for different intensities of external magnetic field. Input beams both with I $\approx$ 10 mW/cm^2. All curves are normalized and the data comes from the $2\vec{k}_a$ - $\vec{k}_b$ signal.

transition $\left|F_g = 2\right\rangle \rightarrow \left|F'_e = 3\right\rangle$ shifts only 0.23 MHz per Gauss [26]. Therefore the detuning achieved with the maximum field is negligible because of the several tens of MHz width of the signal. It is not straightforward to achieve higher fields with our Faraday cage because it was planned to deal only with the earth's magnetic field, which is typically 0.25 G at the laboratory location.

3.6 Scanning speed and direction

Up until this point, all experimental results were taken with a ramp that went from high energies to low energies, henceforth called *down* ramp. We have done this way so that the closed transition would come before the other two in the time window used to detect the FWM signal. However, it is important to discuss what is the influence of this ramp direction in our result. The ramp going from low energies to high energies will be called *up* ramp.

We present in Fig. 25 results for three intensities of the input beams and in both ramp directions. Apparently the asymmetry in the down ramp signal is much more pronounced. The reader must keep in mind that all previous results were taken with this down ramp, so they all have this same asymmetry. The peak relation even inverts in the result for $I_a = I_b = 2.5$ mW/cm^2 in Fig. 25, where the peak in the high energy side is the taller one, a feature only seen for the up ramp. The wings of the signal are also clearly different. Therefore, the broadening and line shape are partially due to the ramp direction, an evidence that there is a temporal dynamics playing a role in the FWM process.

Naturally, we should also check the influence of the ramp speed on the signal. Therefore,

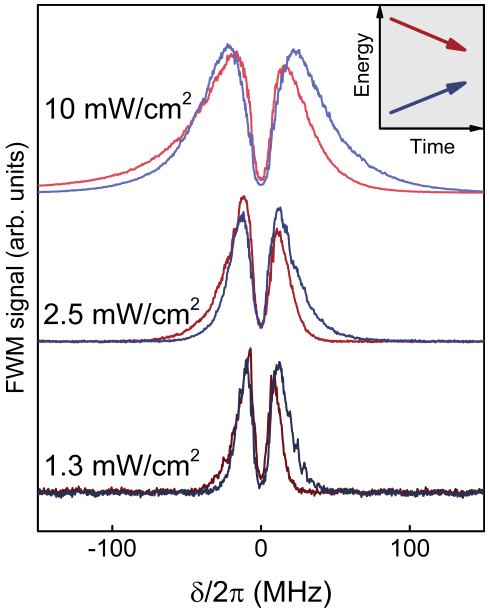

Figure 25 – FWM spectra for three intensities of the input beams and two directions of the scanning ramp. The values next to each curve are the intensities of each input beam. All curves are normalized and the data comes from the $2\vec{k}_a$ - $\vec{k}_b$ signal.

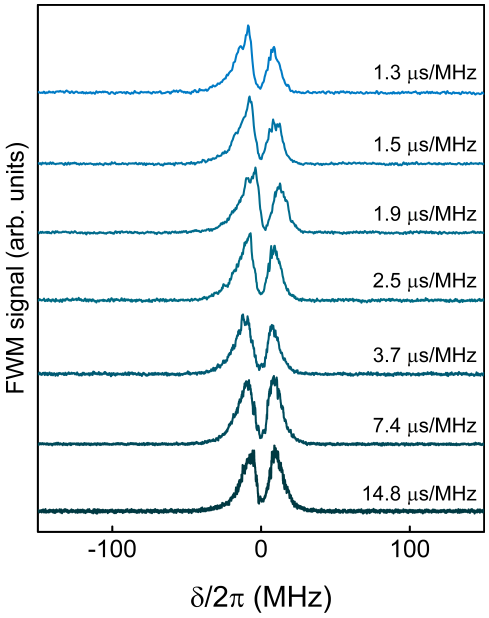

Figure 26 – FWM spectra for several speeds of the ramp. Over each curve we present the time taken to scan 1 MHz. Input beams both with I $\approx$ 1.3 mW/cm^2. All curves are normalized and the data comes from the $2\vec{k}_a$ - $\vec{k}_b$ signal.

using our typical down ramp, we have taken several spectra for different amplitudes of the ramp. This result is given in Fig. 26. To change the amplitude of the ramp is to change its speed because the frequency is fixed and given by the size of time window (250 Hz). In this result it is cleat that, although all usual features are there including the valley, the asymmetry is much less pronounced for slower ramps. This means that the asymmetry might not be due to the light pushing the atoms, since for slower ramps there are more resonant photons. We must remember that according to our estimation of the last chapter, this results were taken in a situation where there is not enough photons to push the atoms out of resonance.

These features, presented in Fig. 25 and 26 support the hypothesis that there must be some temporal dynamics in the FWM signal, given the experimental conditions we use. While the ramp direction affects the broadening, the ramp speed may increase the asymmetry of the peaks. Finally, it is important to notice that even though these ramp parameters, direction and speed, can influence the signal, they do not provoke significant changes in the valley around the resonance.

4 THEORETICAL MODELING AND ANALYSIS

Our goal is to build a theoretical model that gives evidence of the underlying physical mechanism playing a role in the FWM spectra. Then, we present several theoretical results and discuss their agreement with the experimental data.

4.1 Bloch equations

We write down the Bloch equations for a four-level system in which there are two pairs of degenerate levels following our previous analyses in section 3.4. Three fields, initially set as different, interact with the levels in two different orders to generate the $2\vec{k}_a - \vec{k}_b$, as shown in Fig. 27. Each of these options ($\omega_{s-} = \omega_a - \omega_{b+} + \omega_{a'}$ or $\omega_{s+} = \omega_{a'} - \omega_{b-} + \omega_a$) correspond to one circular polarization of the FWM signal. Together, these two add up to a linear polarization.

We shall focus on system I since it should be easy to obtain the solution of system II by analogy. Therefore, the main goal is to obtain the coherence between levels $|1\rangle$ and $|4\rangle$, which contains information about the FWM generated signal. We must emphasize that, once we assume $\omega_a = \omega_{a'}$, the labels of the fields in Fig. 27 follow the convention set up previously and hence, we are modeling the $2\vec{k}_a - \vec{k}_b$ signal. There is no reason to believe that the other signal $2\vec{k}_b - \vec{k}_a$ should be any different, as shown in section 3.1.

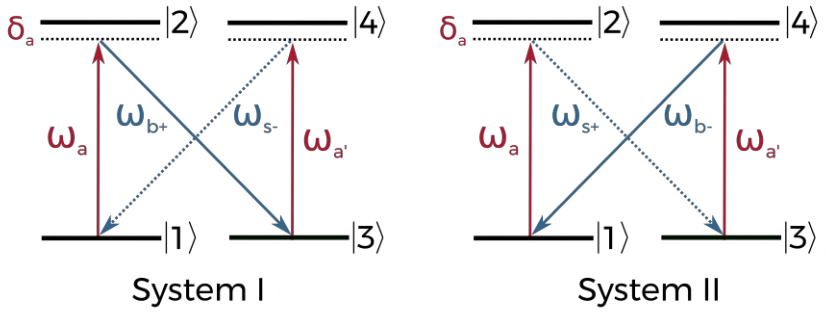

Figure 27 – Schematic representation of the four-level system interacting with three fields. ω_a and $\omega_{a'}$ represent the two photons given by input beam a; ω_{b+} or ω_{b-} represent the one photon stimulated by input beam b; ω_{s+} or ω_{s-} are the two circular components of FWM signal that add up to a linear polarization.

We begin our treatment by writing down the hamiltonian of the system

$$\hat{H} = \hat{H}_0 + \hat{H}_{int}, \tag{14}$$

where $\hat{H}_0$ is the free atom hamiltonian and $\hat{H}_{int}$ is the interaction hamiltonian. At this point, it is necessary to use a few approximations. The first one is to use a semiclassic treatment, i.e. the atoms will have quantized levels while the fields will be classic. Given that, we may also

say that the relevant interaction term of the atoms with the light is the electric dipole, since the wavelength of our lasers is much larger than the atom itself. Completing this initial set of considerations, there is only one electron available to interact with the light, since Rubidium is an alkaline metal. Thus, the interaction hamiltonian is

$$\hat{H}_{int} = -e\vec{r}\cdot\vec{E}_j, \tag{15}$$

where e is the electron charge, $\vec{r}$ is the position vector and $\vec{E}_j$ is the electric field with $j = a, a', b_+, s_-$.

We define the following convention for the fields polarization direction: $\vec{E}_a = E_a\hat{z}$ and $\vec{E}_b = E_b\hat{x}$. Hence, the direction of propagation is $\hat{y}$, while the quantization axis is chosen as $\hat{z}$. Given that, we must rewrite the polarization of the fields in terms of the $\{\pi, \sigma^+, \sigma^-\}$ basis. We know that

$$\begin{aligned}\hat{z} &= \hat{\pi},\\ \hat{x} &= \frac{\sqrt{2}}{2}\left(\hat{\sigma}^+ + \hat{\sigma}^-\right).\end{aligned}$$

As a consequence the fields can be written as

$$\begin{aligned}\vec{E}_a &= \frac{1}{2}\left[\varepsilon_a(t)e^{-i(\omega_a t - k_a y)} + c.c.\right]\hat{\pi},\\ \vec{E}_{a'} &= \frac{1}{2}\left[\varepsilon_{a'}(t)e^{-i(\omega_{a'} t - k_{a'} y)} + c.c.\right]\hat{\pi},\\ \vec{E}_{b+} &= \frac{1}{2}\left[\varepsilon_{b+}(t)e^{-i(\omega_{b+} t - k_{b+} y)} + c.c.\right]\hat{\sigma}^+,\\ \vec{E}_{s-} &= \frac{1}{2}\left[\varepsilon_{s-}(t)e^{-i(\omega_{s-} t - k_{s-} y)} + c.c.\right]\hat{\sigma}^-,\end{aligned} \tag{16}$$

where ε_j is the field amplitude, ω_j is the field frequency and k_j is the wavevector, with $j = a, a', b_+, s_-$.

The field amplitudes do not have any spatial dependence because we have used the approximation that the wavelength is much larger than the atom. Finally, we define the transition dipole moment and the Rabi frequency, respectively, as

$$\mu_{np} = e\left\langle n\left|\vec{r}\cdot\hat{e}_j\right|p\right\rangle, \tag{17}$$

$$\Omega_j = \frac{\mu_{np}\varepsilon_j}{2\hbar}, \tag{18}$$

where $\hat{e}_j$ is the polarization direction of any given field.

With these definitions available, the first task is to calculate all the elements of the interaction hamiltonian. First, notice that all elements in the main diagonal must be zero, because there is no dipole interaction of a level with itself:

$$H_{int,nn} = 0; \qquad n = 1,2,3,4. \tag{19}$$

Let us calculate then the off-diagonal terms

$$H_{int,12} = -\frac{e\langle 1|\vec{r}\cdot\vec{\pi}|2\rangle}{2}\varepsilon_a^*(t)e^{i(\omega_a t - k_a y)} = \frac{-\mu_{12}}{2}\varepsilon_a^*(t)e^{i(\omega_a t - k_a y)}, \tag{20}$$

$$H_{int,13} = 0, \tag{21}$$

$$H_{int,14} = -\frac{e\langle 1|\vec{r}\cdot\vec{\sigma}^-|4\rangle}{2}\varepsilon_{s-}^*(t)e^{i(\omega_{s-} t - k_{s-} y)} = \frac{-\mu_{14}}{2}\varepsilon_{s-}^*(t)e^{i(\omega_{s-} t - k_{s-} y)}, \tag{22}$$

$$H_{int,23} = -\frac{e\langle 2|\vec{r}\cdot\vec{\sigma}^+|3\rangle}{2}\varepsilon_{b+}(t)e^{-i(\omega_{b+} t - k_{b+} y)} = \frac{-\mu_{23}}{2}\varepsilon_{b+}(t)e^{-i(\omega_{b+} t - k_{b+} y)}, \tag{23}$$

$$H_{int,24} = 0, \tag{24}$$

$$H_{int,34} = -\frac{e\langle 3|\vec{r}\cdot\vec{\pi}|4\rangle}{2}\varepsilon_{a'}^*(t)e^{i(\omega_{a'} t - k_{a'} y)} = \frac{-\mu_{34}}{2}\varepsilon_{a'}^*(t)e^{i(\omega_{a'} t - k_{a'} y)}. \tag{25}$$

It is important to notice that only one of the fields components is used in each term. This is done to take in account only the effects of interest, e.g. $|1\rangle \to |2\rangle$ is an absorption process while $|2\rangle \to |3\rangle$ is an emission. The term connecting the ground states $H_{int,13}$ is zero because there is no field directly between them. The same applies to the term between excited states $H_{int,24}$. We may write the complete hamiltonian as

$$\hat{H} = \begin{pmatrix} \mathbb{E}_1 & \frac{-\mu_{12}}{2}\varepsilon_a^*(t)e^{i(\omega_a t - k_a y)} & 0 & \frac{-\mu_{14}}{2}\varepsilon_{s-}^*(t)e^{i(\omega_{s-} t - k_{s-} y)} \\ \frac{-\mu_{12}^*}{2}\varepsilon_a(t)e^{-i(\omega_a t - k_a y)} & \mathbb{E}_2 & \frac{-\mu_{23}}{2}\varepsilon_{b+}(t)e^{-i(\omega_{b+} t - k_{b+} y)} & 0 \\ 0 & \frac{-\mu_{23}^*}{2}\varepsilon_{b+}^*(t)e^{i(\omega_{b+} t - k_{b+} y)} & \mathbb{E}_3 & \frac{-\mu_{34}}{2}\varepsilon_{a'}^*(t)e^{i(\omega_{a'} t - k_{a'} y)} \\ \frac{-\mu_{14}^*}{2}\varepsilon_{s-}(t)e^{-i(\omega_{s-} t - k_{s-} y)} & 0 & \frac{-\mu_{34}^*}{2}\varepsilon_{a'}(t)e^{-i(\omega_{a'} t - k_{a'} y)} & \mathbb{E}_4 \end{pmatrix}, \tag{26}$$

where $\mathbb{E}_i$ with $i = 1,2,3,4$ are the eigenenergies of each level. To write the Bloch equations we must use the density-matrix formalism. To do so we apply Liouville's equation:

$$\frac{\partial\hat{\rho}}{\partial t} = \frac{i}{\hbar}\left[\hat{\rho},\hat{H}\right] + \textit{Relaxation terms}, \tag{27}$$

with $\hat{\rho}$ being the density-matrix operator, ρ_{ii} being the populations of each level and ρ_{ij} the coherence between them (for $i \neq j$). For now, we will overlook the relaxation terms. By using the completeness relations of the system $\sum_{m=1}^{4} |m\rangle \langle m| = 1$ we obtain

$$\frac{\partial \rho_{np}}{\partial t} = \frac{i}{\hbar}(\rho_{n1}H_{1p} + \rho_{n2}H_{2p} + \rho_{n3}H_{3p} + \rho_{n4}H_{4p} - \rho_{1p}H_{n1} - \rho_{2p}H_{n2} - \rho_{3p}H_{n3} - \rho_{4p}H_{n4}). \quad (28)$$

Putting together Eqs. (28) and (26) allows to write down all the populations and coherences as

$$\begin{aligned}\frac{\partial \rho_{11}}{\partial t} = \frac{i}{\hbar}\Bigg(&-\frac{\rho_{12}\mu_{12}^*}{2}\varepsilon_a(t)e^{-i(\omega_a t - k_a y)} + \frac{\rho_{12}^*\mu_{12}}{2}\varepsilon_a^*(t)e^{i(\omega_a t - k_a y)} \\ &- \frac{\rho_{14}\mu_{14}^*}{2}\varepsilon_{s-}(t)e^{-i(\omega_{s-} t - k_{s-} y)} + \frac{\rho_{41}\mu_{14}}{2}\varepsilon_{s-}^*(t)e^{i(\omega_{s-} t - k_{s-} y)}\Bigg),\end{aligned} \quad (29)$$

$$\begin{aligned}\frac{\partial \rho_{22}}{\partial t} = \frac{i}{\hbar}\Bigg(&-\frac{\rho_{12}^*\mu_{12}}{2}\varepsilon_a^*(t)e^{i(\omega_a t - k_a y)} + \frac{\rho_{12}\mu_{12}^*}{2}\varepsilon_a(t)e^{-i(\omega_a t - k_a y)} \\ &- \frac{\rho_{23}\mu_{23}^*}{2}\varepsilon_{b+}^*(t)e^{i(\omega_{b+} t - k_{b+} y)} + \frac{\rho_{23}^*\mu_{23}}{2}\varepsilon_{b+}(t)e^{-i(\omega_{b+} t - k_{b+} y)}\Bigg),\end{aligned} \quad (30)$$

$$\begin{aligned}\frac{\partial \rho_{33}}{\partial t} = \frac{i}{\hbar}\Bigg(&-\frac{\rho_{23}^*\mu_{23}}{2}\varepsilon_{b+}(t)e^{-i(\omega_{b+} t - k_{b+} y)} + \frac{\rho_{23}\mu_{23}^*}{2}\varepsilon_{b+}^*(t)e^{i(\omega_{b+} t - k_{b+} y)} \\ &- \frac{\rho_{34}\mu_{34}^*}{2}\varepsilon_{a'}(t)e^{-i(\omega_{a'} t - k_{a'} y)} + \frac{\rho_{34}^*\mu_{34}}{2}\varepsilon_{a'}^*(t)e^{i(\omega_{a'} t - k_{a'} y)}\Bigg),\end{aligned} \quad (31)$$

$$\begin{aligned}\frac{\partial \rho_{44}}{\partial t} = \frac{i}{\hbar}\Bigg(&-\frac{\rho_{34}^*\mu_{34}}{2}\varepsilon_{a'}^*(t)e^{i(\omega_{a'} t - k_{a'} y)} + \frac{\rho_{34}\mu_{34}^*}{2}\varepsilon_{a'}(t)e^{-i(\omega_{a'} t - k_{a'} y)} \\ &- \frac{\rho_{41}\mu_{14}}{2}\varepsilon_{s-}^*(t)e^{i(\omega_{s-} t - k_{s-} y)} + \frac{\rho_{14}\mu_{14}^*}{2}\varepsilon_{s-}(t)e^{-i(\omega_{s-} t - k_{s-} y)}\Bigg),\end{aligned} \quad (32)$$

$$\begin{aligned}\frac{\partial \rho_{12}}{\partial t} = \frac{i}{\hbar}\Bigg(&-(\rho_{11} - \rho_{22})\frac{\mu_{12}}{2}\varepsilon_a^*(t)e^{i(\omega_a t - k_a y)} + \rho_{12}(E_2 - E_1) \\ &- \frac{\rho_{13}\mu_{23}^*}{2}\varepsilon_{b+}^*(t)e^{i(\omega_{b+} t - k_{b+} y)} + \frac{\rho_{42}\mu_{14}}{2}\varepsilon_{s-}^*(t)e^{i(\omega_{s-} t - k_{s-} y)}\Bigg),\end{aligned} \quad (33)$$

$$\begin{aligned}\frac{\partial \rho_{13}}{\partial t} = \frac{i}{\hbar}\Bigg(&\rho_{13}(E_3 - E_1) - \frac{\rho_{12}\mu_{23}}{2}\varepsilon_{b+}(t)e^{-i(\omega_{b+} t - k_{b+} y)} - \frac{\rho_{14}\mu_{34}^*}{2}\varepsilon_{a'}(t)e^{-i(\omega_{a'} t - k_{a'} y)} \\ &+ \frac{\rho_{23}\mu_{12}}{2}\varepsilon_a^*(t)e^{i(\omega_a t - k_a y)} + \frac{\rho_{43}\mu_{14}}{2}\varepsilon_{s-}^*(t)e^{i(\omega_{s-} t - k_{s-} y)}\Bigg),\end{aligned} \quad (34)$$

$$\frac{\partial \rho_{14}}{\partial t} = \frac{i}{\hbar}\Bigg(-(\rho_{11}-\rho_{44})\frac{\mu_{14}}{2}\varepsilon^*_{s-}(t)e^{i(\omega_{s-}t-k_{s-}y)} + \rho_{14}(E_4-E_1) \\ -\frac{\rho_{13}\mu_{34}}{2}\varepsilon^*_{a'}(t)e^{i(\omega_{a'}t-k_{a'}y)} + \frac{\rho_{24}\mu_{12}}{2}\varepsilon^*_{a}(t)e^{i(\omega_{a}t-k_{a}y)}\Bigg), \tag{35}$$

$$\frac{\partial \rho_{23}}{\partial t} = \frac{i}{\hbar}\Bigg(-\frac{(\rho_{22}-\rho_{33})\mu_{23}}{2}\varepsilon_{b+}(t)e^{-i(\omega_{b+}t-k_{b+}y)} + \rho_{23}(E_3-E_2) \\ -\frac{\rho_{24}\mu^*_{34}}{2}\varepsilon_{a'}(t)e^{-i(\omega_{a'}t-k_{a'}y)} + \frac{\rho_{13}\mu^*_{12}}{2}\varepsilon_{a}(t)e^{-i(\omega_{a}t-k_{a}y)}\Bigg), \tag{36}$$

$$\frac{\partial \rho_{24}}{\partial t} = \frac{i}{\hbar}\Bigg(\rho_{24}(E_4-E_2) - \frac{\rho_{21}\mu_{14}}{2}\varepsilon^*_{s-}(t)e^{i(\omega_{s-}t-k_{s-}y)} - \frac{\rho_{23}\mu_{34}}{2}\varepsilon^*_{a'}(t)e^{i(\omega_{a'}t-k_{a'}y)} \\ + \frac{\rho_{14}\mu^*_{12}}{2}\varepsilon_{a}(t)e^{-i(\omega_{a}t-k_{a}y)} + \frac{\rho_{34}\mu_{23}}{2}\varepsilon_{b+}(t)e^{-i(\omega_{b+}t-k_{b+}y)}\Bigg), \tag{37}$$

$$\frac{\partial \rho_{34}}{\partial t} = \frac{i}{\hbar}\Bigg(-\frac{(\rho_{33}-\rho_{44})\mu_{34}}{2}\varepsilon^*_{a'}(t)e^{i(\omega_{a'}t-k_{a'}y)} + \rho_{34}(E_4-E_3) \\ -\frac{\rho_{31}\mu_{14}}{2}\varepsilon^*_{s-}(t)e^{i(\omega_{s-}t-k_{s-}y)} + \frac{\rho_{24}\mu^*_{23}}{2}\varepsilon^*_{b+}(t)e^{i(\omega_{b+}t-k_{b+}y)}\Bigg). \tag{38}$$

There are six coherences missing since they are the complex conjugate of the already calculated.

At this point we must introduce the slow variables of the system. To do so, it is necessary to remember that ω_{s-} is the generated frequency and due to energy conservation it can be expressed as $\omega_{s-} = \omega_a - \omega_{b+} + \omega_{a'}$. Let us define the slow coherences as

$$\rho_{12} = \sigma_{12}e^{i(\omega_a t - k_a y)}, \tag{39}$$

$$\rho_{13} = \sigma_{13}e^{i(\omega_a t - k_a y - \omega_{b+} t + k_{b+} y)}, \tag{40}$$

$$\rho_{14} = \sigma_{14}e^{i(\omega_{s-} t - k_{s-} y)}, \tag{41}$$

$$\rho_{23} = \sigma_{23}e^{-i(\omega_{b+} t - k_{b+} y)}, \tag{42}$$

$$\rho_{24} = \sigma_{24}e^{i\left(-\omega_{b+} t + k_{b+} y + \omega_{a'} t - k_{a'} y\right)}, \tag{43}$$

$$\rho_{34} = \sigma_{34} e^{i\left(\omega_{a'} t - k_{a'} y\right)}, \tag{44}$$

These definitions allow us to perform the rotating wave approximation, i.e. neglect all terms that oscillate with high frequencies. By doing so and using the Rabi frequency definition of Eq. (18), we are able to eliminate explicit time dependency of our equations. The last step in mounting the Bloch equations is to add the relaxation terms. These terms come from the system coupling with the vacuum, but in our treatment, they will be added phenomenologically. Consider the following rates:

$\gamma_{np} \rightarrow coherence$,

$\Gamma_{np} \rightarrow population$,

$\gamma' \rightarrow (time\ of\ flight)^{-1}$.

We also define the following detunings:

$\delta_a \equiv \omega_a - \omega_{21}$,

$\delta_{b+} \equiv \omega_{b+} - \omega_{23}$,

$\delta_{a'} \equiv \omega_{a'} - \omega_{43}$.

With these definitions, the final set of equations is:

$$\frac{\partial \rho_{11}}{\partial t} = -i\sigma_{12}\Omega_a + i\sigma_{12}^*\Omega_a^* - i\sigma_{14}\Omega_{s-} + i\sigma_{14}^*\Omega_{s-}^* + \Gamma_{21}\rho_{22} + \Gamma_{41}\rho_{44} - \gamma'\left(\rho_{11} - \rho_{11}^0\right); \tag{45}$$

$$\frac{\partial \rho_{22}}{\partial t} = -i\sigma_{12}^*\Omega_a^* + i\sigma_{12}\Omega_a - i\sigma_{23}\Omega_{b+} + i\sigma_{23}^*\Omega_{b+}^* - (\Gamma_{21} + \Gamma_{23} + \gamma')\rho_{22}; \tag{46}$$

$$\frac{\partial \rho_{33}}{\partial t} = -i\sigma_{23}^*\Omega_{b+}^* + i\sigma_{23}\Omega_{b+} - i\sigma_{34}\Omega_{a'} + i\sigma_{34}^*\Omega_{a'}^* + \Gamma_{23}\rho_{22} + \Gamma_{43}\rho_{44} - \gamma'\left(\rho_{33} - \rho_{33}^0\right); \tag{47}$$

$$\frac{\partial \rho_{44}}{\partial t} = -i\sigma_{34}^*\Omega_{a'}^* + i\sigma_{34}\Omega_{a'} - i\sigma_{14}^*\Omega_{s-}^* + i\sigma_{14}\Omega_{s-} - (\Gamma_{41} + \Gamma_{43} + \gamma')\rho_{44}; \tag{48}$$

$$\frac{\partial \sigma_{12}}{\partial t} = -\sigma_{12}\left(i\delta_a + \gamma_{12} + \gamma'\right) - i(\rho_{11} - \rho_{22})\Omega_a^* - i\sigma_{13}\Omega_{b+}^* + i\sigma_{24}^*\Omega_{s-}^*; \tag{49}$$

$$\frac{\partial \sigma_{13}}{\partial t} = -\sigma_{13}\left(i\delta_a - i\delta_{b+} + \gamma_{13} + \gamma'\right) - i\sigma_{12}\Omega_{b+} - i\sigma_{14}\Omega_{a'}e^{i\Delta ky} + i\sigma_{23}\Omega_a^* + i\sigma_{34}^*\Omega_{s-}^* e^{i\Delta ky}; \tag{50}$$

$$\frac{\partial \sigma_{14}}{\partial t} = -\sigma_{14}\left(i\delta_a - i\delta_{b+} + i\delta_{a'} + \gamma_{14} + \gamma'\right) - i(\rho_{11} - \rho_{44})\Omega^*_{s-} - i\sigma_{13}\Omega^*_{a'}e^{-i\Delta ky} + i\sigma_{24}\Omega^*_a e^{-i\Delta ky}; \tag{51}$$

$$\frac{\partial \sigma_{23}}{\partial t} = -\sigma_{23}\left(-i\delta_{b+} + \gamma_{23} + \gamma'\right) - i(\rho_{22} - \rho_{33})\Omega_{b+} - i\sigma_{24}\Omega_{a'} + i\sigma_{13}\Omega_a; \tag{52}$$

$$\frac{\partial \sigma_{24}}{\partial t} = -\sigma_{24}\left(-i\delta_{b+} + i\delta_{a'} + \gamma_{24} + \gamma'\right) - i\sigma^*_{12}\Omega^*_{s-}e^{i\Delta ky} - i\sigma_{23}\Omega^*_{a'} + i\sigma_{14}\Omega_a e^{i\Delta ky} + i\sigma_{34}\Omega_{b+}; \tag{53}$$

$$\frac{\partial \sigma_{34}}{\partial t} = -\sigma_{34}\left(i\delta_{a'} + \gamma_{34} + \gamma'\right) - i(\rho_{33} - \rho_{44})\Omega^*_{a'} - i\sigma^*_{13}\Omega^*_{s-}e^{i\Delta ky} + i\sigma_{24}\Omega^*_{b+}. \tag{54}$$

In these last equations we used the definition $\omega_{np} \equiv \frac{\mathbb{E}_n - \mathbb{E}_p}{\hbar}$ and $\Delta k \equiv k_a + k_{a'} - k_{b+} - k_{s-}$, assuming that the input beams are collinear.

4.2 Steady-state solution

With the Bloch equations set up, the next task is to solve them. We look for a steady-state solution, since we assume that the intrinsic dynamics of the atoms interacting with light is much faster than our lasers scan speed. With that in mind, we zero out all time derivatives:

$$\rho_{11} = \frac{-i\sigma_{12}\Omega_a + i\sigma^*_{12}\Omega^*_a - i\sigma_{14}\Omega_{s-} + i\sigma^*_{14}\Omega^*_{s-} + \Gamma_{21}\rho_{22} + \Gamma_{41}\rho_{44} + \gamma'\rho^0_{11}}{\gamma'}; \tag{55}$$

$$\rho_{22} = \frac{-i\sigma^*_{12}\Omega^*_a + i\sigma_{12}\Omega_a - i\sigma_{23}\Omega_{b+} + i\sigma^*_{23}\Omega^*_{b+}}{\Gamma_{21} + \Gamma_{23} + \gamma'}; \tag{56}$$

$$\rho_{33} = \frac{-i\sigma^*_{23}\Omega^*_{b+} + i\sigma_{23}\Omega_{b+} - i\sigma_{34}\Omega_{a'} + i\sigma^*_{34}\Omega^*_{a'} + \Gamma_{23}\rho_{22} + \Gamma_{43}\rho_{44} + \gamma'\rho^0_{33}}{\gamma'}; \tag{57}$$

$$\rho_{44} = \frac{-i\sigma^*_{34}\Omega^*_{a'} + i\sigma_{34}\Omega_{a'} - i\sigma^*_{14}\Omega^*_{s-} + i\sigma_{14}\Omega_{s-}}{\Gamma_{41} + \Gamma_{43} + \gamma}; \tag{58}$$

$$\sigma_{12} = \frac{-i(\rho_{11}-\rho_{22})\Omega_a^* - i\sigma_{13}\Omega_{b+}^* + i\sigma_{24}^*\Omega_{s-}^*}{i\delta_a + \gamma_{12} + \gamma'}; \tag{59}$$

$$\sigma_{13} = \frac{-i\sigma_{12}\Omega_{b+} - i\sigma_{14}\Omega_{a'}e^{i\Delta ky} + i\sigma_{23}\Omega_a^* + i\sigma_{34}^*\Omega_{s-}^* e^{i\Delta ky}}{i\delta_a - i\delta_{b+} + \gamma_{13} + \gamma'}; \tag{60}$$

$$\sigma_{14} = \frac{-i(\rho_{11}-\rho_{44})\Omega_{s-}^* - i\sigma_{13}\Omega_{a'}^* e^{-i\Delta ky} + i\sigma_{24}\Omega_a^* e^{-i\Delta ky}}{i\delta_a - i\delta_{b+} + i\delta_{a'} + \gamma_{14} + \gamma'}; \tag{61}$$

$$\sigma_{23} = \frac{-i(\rho_{22}-\rho_{33})\Omega_{b+} - i\sigma_{24}\Omega_{a'} + i\sigma_{13}\Omega_a}{-i\delta_{b+} + \gamma_{23} + \gamma'}; \tag{62}$$

$$\sigma_{24} = \frac{-i\sigma_{12}^*\Omega_{s-}^* e^{i\Delta ky} - i\sigma_{23}\Omega_{a'}^* + i\sigma_{14}\Omega_a e^{i\Delta ky} + i\sigma_{34}\Omega_{b+}}{-i\delta_{b+} + i\delta_{a'} + \gamma_{24} + \gamma'}; \tag{63}$$

$$\sigma_{34} = \frac{-i(\rho_{33}-\rho_{44})\Omega_{a'}^* - i\sigma_{13}^*\Omega_{s-}^* e^{i\Delta ky} + i\sigma_{24}\Omega_{b+}^*}{i\delta_{a'} + \gamma_{34} + \gamma'}. \tag{64}$$

Given that the main goal is to obtain the FWM signal, we will solve the system for σ_{14} perturbatively. Let us look for solutions in first order of Ω_{b+} and up to second order of Ω_a or $\Omega_{a'}$. It is this particular choice of field orders that contains the right direction in which the signal is generated. We also leave the term related to Ω_{s-} in first order, since it will be used in a later section to investigate absorption effects.

To perform the perturbation we take σ_{14}, as it is in Eq. (61), and substitute the populations and coherences respecting the order restrictions just mentioned. After the first round of substitutions we arrive at

$$\begin{aligned}\sigma_{14}\left((i\delta_a - i\delta_{b+} + i\delta_{a'} + \gamma_{14} + \gamma') + \frac{|\Omega_{a'}|^2}{(i\delta_a - i\delta_{b+} + \gamma_{13} + \gamma')} + \frac{|\Omega_a|^2}{(-i\delta_{b+} + i\delta_{a'} + \gamma_{24} + \gamma')}\right) \\ \cong -i\rho_{11}^0\Omega_{s-}^* - \frac{\sigma_{12}\Omega_{b+}\Omega_{a'}^* e^{-i\Delta ky}}{(i\delta_a - i\delta_{b+} + \gamma_{13} + \gamma')} + \frac{\sigma_{23}\Omega_a^*\Omega_{a'}^* e^{-i\Delta ky}}{(i\delta_a - i\delta_{b+} + \gamma_{13} + \gamma')} \\ + \frac{\sigma_{23}\Omega_{a'}^*\Omega_a^* e^{-i\Delta ky}}{(-i\delta_{b+} + i\delta_{a'} + \gamma_{24} + \gamma')} - \frac{\sigma_{34}\Omega_{b+}\Omega_a^* e^{-i\Delta ky}}{(-i\delta_{b+} + i\delta_{a'} + \gamma_{24} + \gamma')}.\end{aligned} \tag{65}$$

To keep obeying the order restrictions we imposed, we must approximate σ_{12}, σ_{34} and σ_{23}.

$$\sigma_{12} \cong \frac{-i\Omega_a^*}{(i\delta_a + \gamma_{12} + \gamma')}(\rho_{11} - \rho_{22}), \tag{66}$$

$$\sigma_{23} \cong \frac{i\Omega_{b+}}{(-i\delta_{b+} + \gamma_{23} + \gamma')}(\rho_{33} - \rho_{22}), \tag{67}$$

$$\sigma_{34} \cong \frac{-i\Omega_{a'}^*}{(i\delta_{a'} + \gamma_{34} + \gamma')}(\rho_{33} - \rho_{44}). \tag{68}$$

The input lasers are strong enough to move population around the system and not only create coherence. Therefore we will model these population differences in Eqs. (66-68) as if we had two-level systems interacting with a single field. We start with the left half of the system (levels $|1\rangle$ and $|2\rangle$). The other two terms can be solved by analogy. Therefore, using this two-level approximation, the excited state population is

$$\rho_{22} = (\rho_{11} - \rho_{22}) |\Omega_a|^2 \left(\frac{2(\gamma_{12} + \gamma')}{(\Gamma_{21} + \Gamma_{23} - \gamma') \left(\delta_a^2 + (\gamma_{12} + \gamma')^2 \right)} \right). \tag{69}$$

In order to calculate the population difference we make the assumption $\rho_{11} = \rho_{11}^0 = 1$ in Eq. (69). With this consideration the population difference for this left half of the system is

$$\rho_{11} - \rho_{22} = \frac{(\Gamma_{21} + \Gamma_{23} + \gamma') \left(\delta_a^2 + (\gamma_{12} + \gamma')^2 \right) \rho_{11}^0}{(\Gamma_{21} + \Gamma_{23} + \gamma') \left(\delta_a^2 + (\gamma_{12} + \gamma')^2 \right) + 2(\gamma_{12} + \gamma') |\Omega_a|^2}. \tag{70}$$

If we had used the population conservation condition for a two-level system in Eq. (69), there would be an extra factor of 2 in one of the terms of the denominator of Eq. (70) and the zeroth order population would not appear. Finally, we may rewrite Eq. (66) using the result of Eq. (70). It is also possible to rewrite Eqs. (67, 68) by analogy.

At this point it is worth to introduce a small simplification, that is adding the time of flight rate into the coherence loss rate, e.g. $\gamma_{12} + \gamma' \to \gamma_{12}$. We may do so because these rates are always together in the equations. Furthermore, the time of flight rate must be much smaller than any other rate in the system, because we are modelling atoms with very low speeds. With this in mind, the coherence σ_{14} is:

$$\sigma_{14} \cong \left[(i\delta_a - i\delta_{b+} + i\delta_{a'} + \gamma_{14}) + \frac{|\Omega_{a'}|^2}{(i\delta_a - i\delta_{b+} + \gamma_{13})} + \frac{|\Omega_a|^2}{(-i\delta_{b+} + i\delta_{a'} + \gamma_{24})} \right]^{-1} \left[-i\rho_{11}^0 \Omega_{s-}^* \right. \tag{71}$$

$$+ i\Omega_a^* \Omega_{a'}^* \Omega_{b+} e^{-i\Delta ky} \left(\frac{(\Gamma_{21}+\Gamma_{23})\left(\delta_a^2+\gamma_{12}^2\right)\rho_{11}^0}{(i\delta_a+\gamma_{12})(i\delta_a - i\delta_{b+}+\gamma_{13})\left[(\Gamma_{21}+\Gamma_{23})\left(\delta_a^2+\gamma_{12}^2\right)+2|\Omega_a|^2\gamma_{12}\right]} \right.$$

$$+ \frac{(\Gamma_{21}+\Gamma_{23})\left(\delta_b^2+\gamma_{23}^2\right)\rho_{33}^0}{(i\delta_a - i\delta_{b+}+\gamma_{13})(-i\delta_{b+}+\gamma_{23})\left[(\Gamma_{21}+\Gamma_{23})\left(\delta_b^2+\gamma_{23}^2\right)+2|\Omega_b|^2\gamma_{23}\right]}$$

$$+ \frac{(\Gamma_{21}+\Gamma_{23})\left(\delta_b^2+\gamma_{23}^2\right)\rho_{33}^0}{(-i\delta_{b+}+i\delta_{a'}+\gamma_{24})(-i\delta_{b+}+\gamma_{23})\left[(\Gamma_{21}+\Gamma_{23})\left(\delta_b^2+\gamma_{23}^2\right)+2|\Omega_b|^2\gamma_{23}\right]}$$

$$\left. \left. + \frac{(\Gamma_{41}+\Gamma_{43})\left(\delta_{a'}^2+\gamma_{34}^2\right)\rho_{33}^0}{(-i\delta_{b+}+i\delta_{a'}+\gamma_{24})(i\delta_{a'}+\gamma_{34})\left[(\Gamma_{41}+\Gamma_{43})\left(\delta_{a'}^2+\gamma_{34}^2\right)+2|\Omega_{a'}|^2\gamma_{34}\right]} \right) \right].$$

This result can be seen as the main core of our theoretical model. There is no need to go back to the actual coherence ρ_{14} since the FWM signal is equal to the modulus squared of the coherence, apart from constants. It must be emphasized that to take in account propagation effects such as absorption and phase-matching, we still need to connect this coherence with Maxwell's equations. In addition, there is no need to account for Doppler broadening, i.e. integrating in the Maxwell-Boltzmann distribution, since the experiment uses a cold atomic sample.

Before plotting $|\sigma_{14}|^2$ (Eq. (71)), it is important to analyze the four terms inside the parenthesis, the ones with dependency on the ground state populations. Each of these terms come from a different pathway to induce the coherence ρ_{14} and we may map these pathways as shown in Fig. 28. To build this map we kept track of each substitution in the process of solving Eqs. (55-64) and the Rabi frequencies connected with these substitutions.

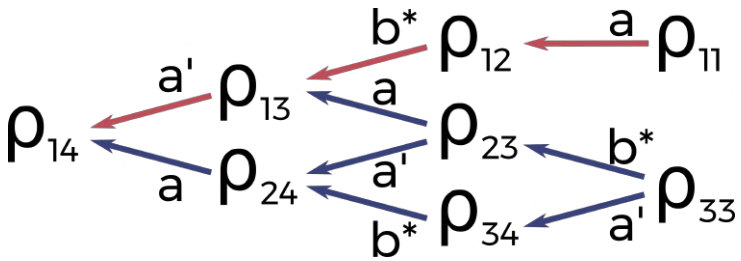

Figure 28 – The four excitation pathways that induce the coherence ρ_{14}.

The red pathway, henceforth labeled *direct pathway*, is the most natural one. It involves an absorption of a photon of the input beam a by an atom in ρ_{11}, creating the coherence ρ_{12}. The input beam b stimulates the emission of a photon to $|3\rangle$ inducing the coherence ρ_{13}. Finally, a second photon from a' is absorbed completing the FWM excitation and creating ρ_{14}. An observant reader will notice that this is an exact description of the process in the system I of Fig. 27.

Our model is showing then, that apart from this straightforward excitation route there are three other more. By carefully analyzing these three pathways, one concludes that they have an eccentric time ordering of the excitations. Let us take the bottom-most pathway in Fig. 28 as an example. It starts with an absorption from an atom in ρ_{33} inducing the coherence ρ_{34}, an absolutely normal process. Following that, there is a stimulated emission from $|2\rangle \rightarrow |3\rangle$ inducing the coherence ρ_{24}. This process seems to follow an unnatural order because there was no previous excitation to level $|2\rangle$ so it could not emit a photon. Problems like this emerge in the other two routes that depend on ρ_{33}.

To further analyze these coherence pathways, let us look at the theoretical results presented in Fig. 29. We have plotted $|\sigma_{14}|^2$ using the complete solution of Eq. (71) and using only the direct pathway, i.e. the term with dependency on ρ_{11}. The rates used in these plots follow the know value of $\Gamma = 6.06$ MHz for the natural linewidth of the D_2 line of ^{87}Rb [26]. Thus the coherence decay rates between excited and ground state levels are $\Gamma/2$. As for the rates γ_{13} and γ_{24}, we expect them to be much smaller than all other rates because these coherences between the two ground states or between the two excited states should last much longer. So they are set as two orders smaller.

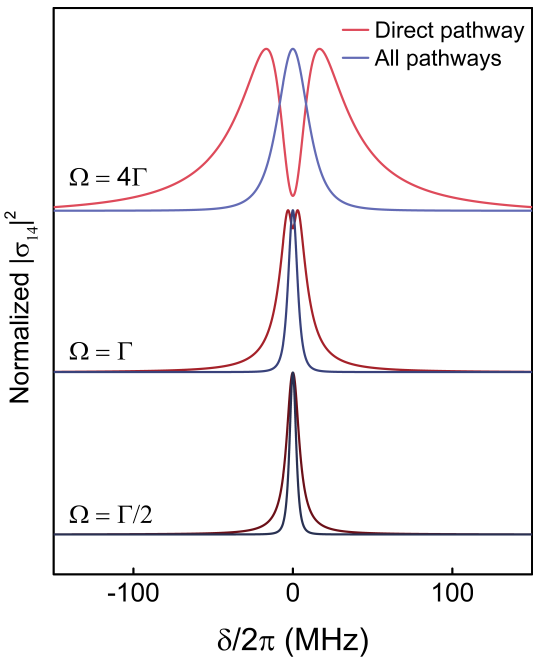

Figure 29 – Theoretical results for the FWM signal without absorption for three intensities of the input lasers using the complete solution (blue) and only the direct pathway (red).The Rabi frequency of each input beam is Ω. All curves are normalized.

The complete solution (in blue in Fig. 29) is a single peak that broadens with the increasing intensity. On the other hand, with the solution containing only the direct pathway there is a deep valley for high intensities. This seems to agree, at least partially, with the experimental results. In order to understand the nature of this valley in the direct pathway solution we must look at the real and imaginary parts, since the modulus squared is actually the sum of the square

of these terms. This result is presented in Fig. 30 for the same three intensities of the previous graph.

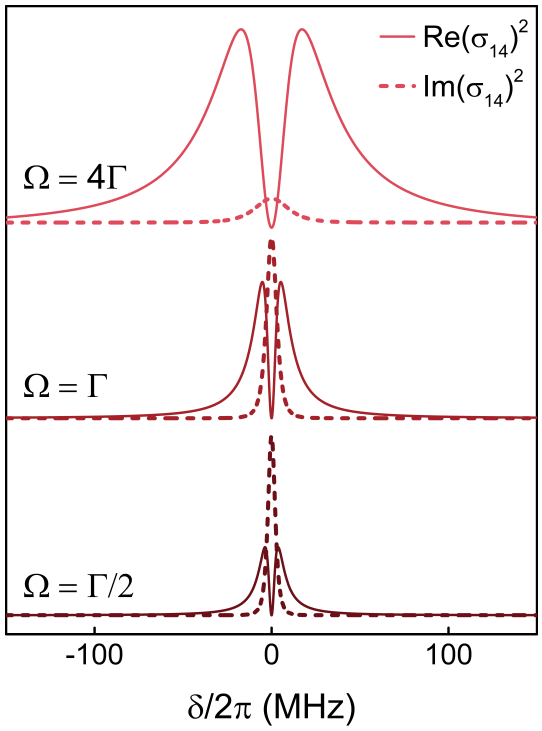

Figure 30 – Real (solid) and imaginary (dashed) parts of the direct pathway solution for three different intensities. The Rabi frequency of each input beam is Ω.

Although we are not calculating the electric susceptibility, which is the medium response to the action of light, we know that it should be very similar to the square modulus of the coherence, apart from absorption and phase-matching. We also know that the real part alone of the electric susceptibility is a curve with a zero on the resonance. This is a known result for the dispersion near the resonance of a medium [15]. Therefore, once we take the square of this real part, it must have a valley with the minimum precisely on zero.

Thus, for the results presented in Fig. 30, the valley arises for high intensities because the real part has become larger than the imaginary part. This is also the same reason why there is not a valley in the complete solution, because the imaginary part is always several orders larger than the real part. It seems then, that at least for high intensities we can explain the valley in the FWM spectrum as a result of dispersion. This type of dispersive response was already observed in a Doppler-broadened FWM in a phase-conjugation configuration [32]. Since the direct pathway solution agrees at some level with experimental data and it has reasonable temporal ordering, we will neglect the other three pathways from now on. However, it is still imperative to find a solid physical reasoning to drop out these terms.

To explain the low intensity regime we must connect the solution of our model with the Maxwell's equations. We expect that once absorption or phase-matching effects are considered, a complete agreement can be achieved.

4.3 Connection with the Electromagnetism

By uncoupling Maxwell's equations using the standard methods one arrives at a wave equation. The solution of this wave equation connected to our model is the object of interest of this section. We already start from a simple version of the equation, where all transverse dependency was neglected [33]:

$$\frac{\partial^2 E_{s-}}{\partial y^2} - \frac{1}{c^2}\frac{\partial^2 E_{s-}}{\partial t^2} = \frac{1}{\varepsilon_0 c^2}\frac{\partial^2 P}{\partial t^2}. \tag{72}$$

Where E_{s-} is the generated FWM electric field; c is the speed of light in the vacuum; ε_0 is the vacuum permittivity and P is the polarization induced in the medium.

We are interested in the polarization that oscillates with the FWM frequency, i.e. ω_{s-}, therefore [33]

$$P(\omega_{s-}) = NTr(\rho\mu) = N\mu_{14}\rho_{41}. \tag{73}$$

We may write the polarization without the complex conjugate term because of the rotating wave approximation, i.e. to avoid fast oscillating terms. Therefore, from our previous definition, Eq. (41):

$$P(\omega_{s-}) = N\mu_{14}\sigma_{41}e^{-i(\omega_{s-}t - k_{s-}y)}. \tag{74}$$

At this point we must introduce several approximations. These are:

- Steady-state regime of the coherence, i.e. time derivatives of σ_{41} are zero;
- Adiabatic approximation: $\left|\frac{\partial^2 \varepsilon_{s-}(y,t)}{\partial y^2}\right| \ll \left|k_{s-}\frac{\partial \varepsilon_{s-}(y,t)}{\partial y}\right|$, where $k_{s-} = \omega_{s-}/c$ is the wavevector of FWM light;
- The field amplitude ε_{s-} is constant.

By substituting Eq. (74) in Eq. (72) with all these approximations we arrive at the much simpler result:

$$\frac{\partial \varepsilon_{s-}(y,t)}{\partial y} = \frac{i\omega_{s-}N\mu_{14}}{\varepsilon_0 c}\sigma_{41}. \tag{75}$$

If we multiply both sides of Eq. (75) by $\mu_{14}/2\hbar$, the left side becomes the Rabi frequency:

$$\frac{\partial \Omega_{s-}}{\partial y} = \frac{i\omega_{s-}N\mu_{14}^2}{2\hbar\varepsilon_0 c}\sigma_{41}. \tag{76}$$

Our model gives σ_{41}, which is merely the complex conjugate of σ_{14} (Eq. (71)). At this point, it is interesting to ease our heavy notation. We substitute Eq. (71) in Eq. (76) by incorporating all the constants inside A and B parameters. They are huge parts of Eq. (71) and mostly contain detunings and the Rabi frequencies. The first one contains all terms with no dependency on Ω_{s-} and will account for the phase-matching, while the second contains the single term Ω_{s-} dependent and will account for the absorption of the generated light. Our equation finally becomes

$$\frac{\partial \Omega_{s-}}{\partial y} = Ae^{i\Delta k y} + B\Omega_{s-}. \tag{77}$$

This is a fairly simple ordinary differential equation to solve if we perform the change of variables $\Omega'_{s-} = \Omega_{s-}e^{-i\Delta k y}$. With the general solution on hands, we impose the condition $\Omega_{s-}(y=0) = 0$, a fair condition since no signal must be generated at the very beginning of the sample, rendering

$$\Omega_{s-} = \frac{A}{(B - i\Delta k)}\left(e^{BL} - e^{i\Delta k L}\right), \tag{78}$$

where L is the sample size.

This equation allow us to probe the action of the absorption of the generated light (parameter B) or the phase matching condition Δk separately. For the moment, we will assume the phase matching condition to be fulfilled, i.e. $\Delta k = 0$. In a later section there is a discussion about the effect of this condition on the result. Before plotting the results, let us add the absorption of the input beams.

We may model this absorption using Eqs. (66-68), i.e. assuming that the lasers interact with two-level systems. Then, we follow the same procedure with the wave equation to arrive at the following results:

$$\Omega_a = \Omega_a^0 e^{-\frac{k_a N \mu_{21}^2 L}{2\hbar\varepsilon_0}\frac{\rho_{11}^0}{(-i\delta_a+\gamma_{12})}\frac{(\Gamma_{21}+\Gamma_{23})\left(\delta_a^2+\gamma_{12}^2\right)}{(\Gamma_{21}+\Gamma_{23})\left(\delta_a^2+\gamma_{12}^2\right)+2\gamma_{12}|\Omega_a|^2}}; \tag{79}$$

$$\Omega_{a'} = \Omega_{a'}^0 e^{-\frac{k_{a'} N \mu_{43}^2 L}{2\hbar\varepsilon_0}\frac{\rho_{33}^0}{\left(-i\delta_{a'}+\gamma_{34}\right)}\frac{(\Gamma_{41}+\Gamma_{43})\left(\delta_{a'}^2+\gamma_{34}^2\right)}{(\Gamma_{41}+\Gamma_{43})\left(\delta_{a'}^2+(\gamma)^2\right)+2\gamma_{34}\left|\Omega_{a'}\right|^2}}; \tag{80}$$

$$\Omega_{b+} = \Omega_{b+}^0 e^{-\frac{k_{b+} N \mu_{23}^2 L}{2\hbar\varepsilon_0}\frac{\rho_{33}^0}{(-i\delta_{b+}+\gamma_{23})}\frac{(\Gamma_{21}+\Gamma_{23})\left(\delta_b^2+\gamma_{23}^2\right)}{(\Gamma_{21}+\Gamma_{23})\left(\delta_b^2+\gamma_{23}^2\right)+2\gamma_{23}|\Omega_b|^2}}. \tag{81}$$

To add the absorption of the input beams is to change their Rabi frequencies in all previous equations with these last three (Eqs. (78-80)). With this, it is possible to plot the FWM spectrum, given by the direct pathway solution (see red curve in Fig. 29), in four different situations: (i)

without any absorption; (ii) with absorption of the input beams; (iii) with absorption of the generated light; (iv) with both absorption effects. In Fig. 31 we present these four configuration for different regimes of intensity of the input beams. A few extra parameters were necessary to plot these results. The dipole moments are available in Ref. [26]. As for the number of atoms and MOT diameter, they were set as $N = 5 \times 10^9$ atoms and d = 4 mm, the typical values of our experimental setup as described in chapter 2.

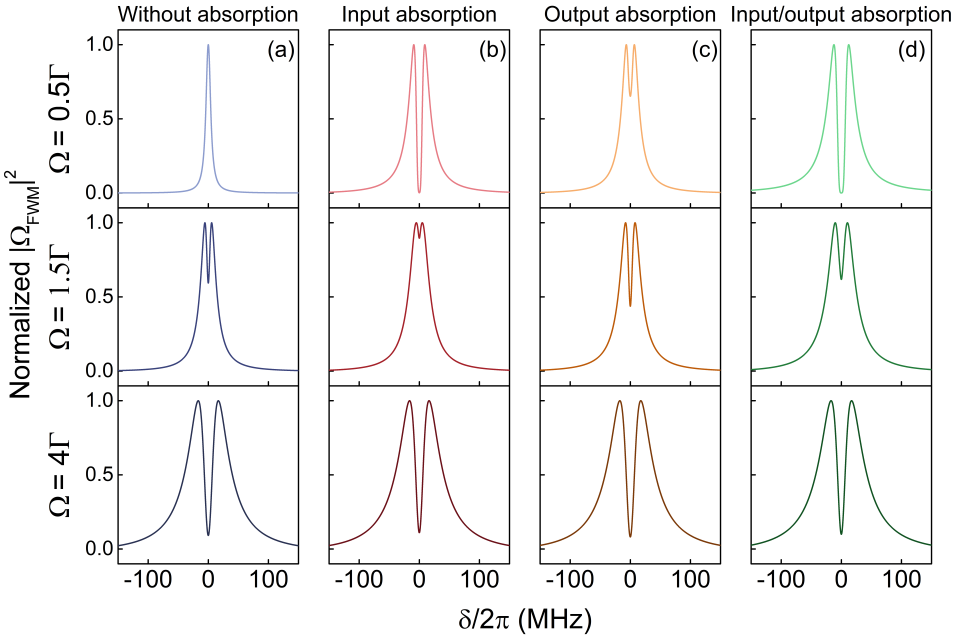

Figure 31 – Theoretical FWM spectra for different absorption configurations and intensities of the input beams. The Rabi frequency of each input beam is Ω. All curves are normalized.

The results presented in Fig. 31 show a clear picture of the successes and failures of the theoretical model. For a low intensity regime the valley is mainly due to absorption of the input beams, which is a quite reasonable result. It is expected that the medium absorbs more efficiently weaker beams. For a high intensity regime, the previous analysis in section 4.2 already showed that the growth of the real part of the induced coherence, i.e. the dispersion, could explain the valley. It remains to understand what happens near the saturation intensity. It seems that for this regime the absorption is no longer enough to explain the depth of the valley, while the dispersion has not yet started.

In this context, it might give us some insight to look at the behavior of the depth of the valley for the different intensities of the input beams. This parameter for both theory and experiment is presented in Fig. 32. The theoretical data confirms the behavior seen in Fig. 31, i.e. the valley depth decreases drastically around the saturation intensity. While this is a $\approx 60\%$ fall for the theoretical data, in the experiment there is a moderate change in the depth around the saturation intensity, approximately 10%. Thus, even if the experimental valley depth is much more robust regarding intensity variations, it has a slightly similar behavior to the theoretical

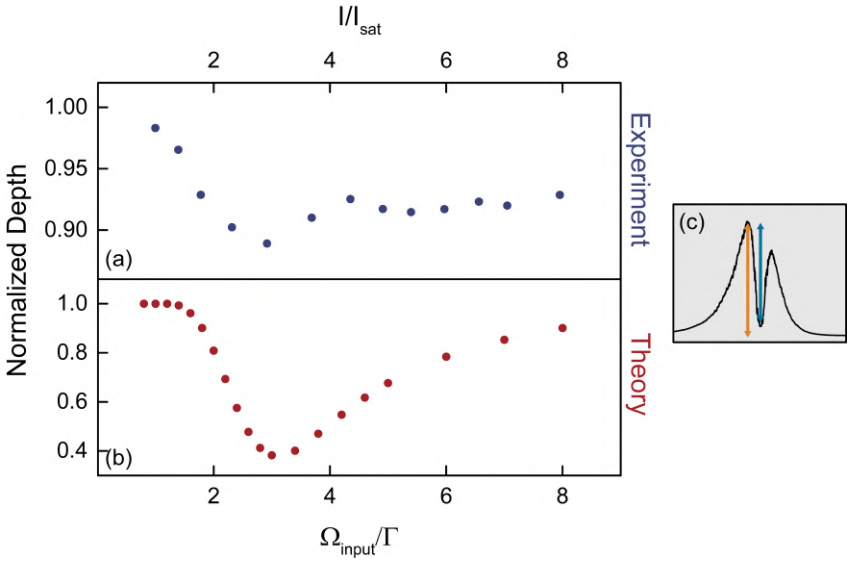

Figure 32 – Normalized valley depth with (a) experimental data as a function of total intensity $I = I_a + I_b$ and (b) theoretical data as a function of $\Omega_{input} = \Omega_a + \Omega_b$. (c) The normalized depth is the depth (turquoise) divided by the amplitude (orange).

result. This is not a strong evidence, but it might point out that our model is not in the wrong direction.

To support the interpretation that in a high intensity regime the valley is due to the real part of the Rabi frequency, and therefore is connected to dispersion effects, let us compare the complete solution and the direct solution including absorption of the input beams and of the generated light. This result is presented in Fig. 33 and it has similar conditions to the one of Fig. 29.

It is clear that the absorption is able to explain the valley for a low intensity regime, given that both solutions present such a valley. However, for intensities higher than the saturation intensity, only the direct solution keeps presenting the valley. This confirms the decision we took in the model of considering only the direct excitation pathway. In addition, it also strengthens the interpretation of dispersion effects for high intensities.

There are other features that the model should be able to provide. One of those is the line shape. Fig. 34 shows a superposition of three FWM spectra produced by the theoretical and experimental data. For the theoretical results, we use the model of Fig. 31 (d), i.e. considering the absorption of the input beams and the generated light. As the experimental results, they were taken with the typical scanning parameters, i.e. down ramp with a frequency of 250 Hz and a 3 V amplitude.

The wings of the spectra are noticeably different in shape, whereas the width presents good agreement. The experimental asymmetry, specially in the wings, seems to come from the frequency scanning of the laser, as discussed in section 3.6. Apart from this disagreement, there is a similarity between the curves that once again shows that the model does achieve some

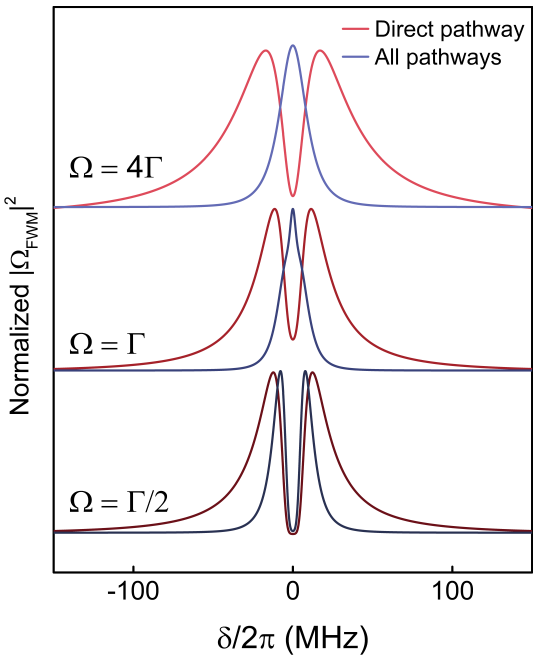

Figure 33 – Theoretical results for the FWM signal with input/output absorption for three intensities of the input lasers using the complete solution (blue) and only the direct pathway (red). The Rabi frequency of each input beam is Ω. All curves are normalized.

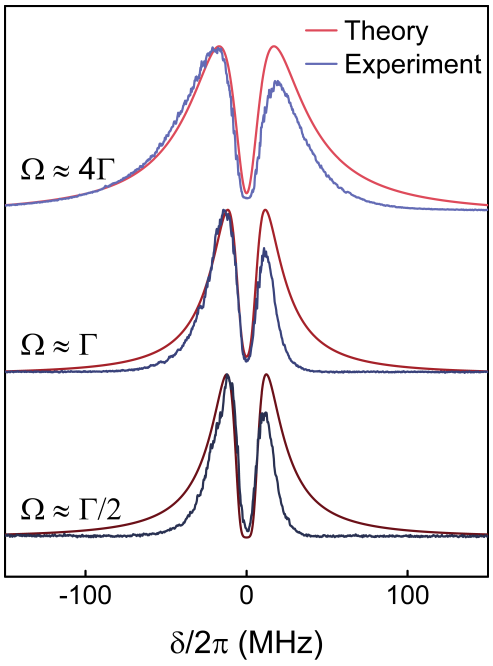

Figure 34 – Comparison between experimental and theoretical FWM spectra for three different intensities of the input beams. The Rabi frequency of each input beam is Ω. All curves are normalized.

success. This similarity presents itself specially in the valley line shape and width.

4.4 Phase matching

In the last attempt to complete the theoretical model, the phase matching condition must be considered. In all theoretical results so far, this condition was assumed to be fulfilled, i.e. $\Delta k = 0$. In this section, we calculate $\Delta\vec{k}$ and show its impact on the FWM spectra. From the geometry of the experiment, we know that there is a small angle between the input beams. This angle must be taken in account when calculating the phase matching.

$$\begin{aligned}\Delta k &= \vec{k}_a + \vec{k}_{a'} + \vec{k}_{b+} + \vec{k}_{s-} \\ &= k_a + k_{a'} - k_{b+}cos(\theta) - k_{s-}cos(\theta) \\ &= \frac{n_a}{c}(\omega_a + \omega_{a'}) - \frac{n_b cos(\theta)}{c}(\omega_{b+} + \omega_{s-}).\end{aligned} \tag{82}$$

The input beams a and b experience the indexes of refraction n_a and n_b, respectively. We assume that these indexes depend on the real part of the first order coherence associated to their respective transitions. Finally, we use the energy conservation to rewrite $\omega_{s-} = \omega_a + \omega_{a'} - \omega_{b+}$. The index of refraction may be written as:

$$n_a = n_b = 1 + 2\pi Re\chi^{(1)}. \tag{83}$$

Given these considerations the final form of the phase matching condition is

$$\Delta k = \frac{\omega_a + \omega_{a'}}{c}\left(1 + \frac{2\pi N\mu_{12,\pi}^2}{2\hbar\varepsilon_0}\frac{\delta_a}{\delta_a^2 + (\gamma_{12} + \gamma')^2} - cos(\theta)\left(1 + \frac{2\pi N\mu_{23,\sigma}^2}{2\hbar\varepsilon_0}\frac{\delta_{b+}}{\delta_{b+}^2 + (\gamma_{23} + \gamma')^2}\right)\right). \tag{84}$$

In the final FWM spectra, the phase matching plays a role as the argument of a $sinc^2(\Delta kL)$ function. This is a consequence of taking the modulus squared of Eq. (78). Thus, for the correct parameters, e.g. angle between input beams and atomic density, the phase matching condition might modulate the spectrum introducing an asymmetry. The experimental angle was fixed at 10 mrad, as mentioned in chapter 2. Hence the only parameter that may fluctuate is the atomic density because of the unlocked cooling and repumping lasers. We present the theoretical FWM spectrum for three different number of atoms in the MOT in Fig. 36. These curves use the model of Fig. 31 (d), with both absorption effects.

These results show that the phase matching condition might introduce an asymmetry in the FWM spectra, but with great sensibility to the atomic density. In fact, with the parameter that was used in the previous result, $N = 5 \times 10^9$ atoms, the typical number of atoms in the system,

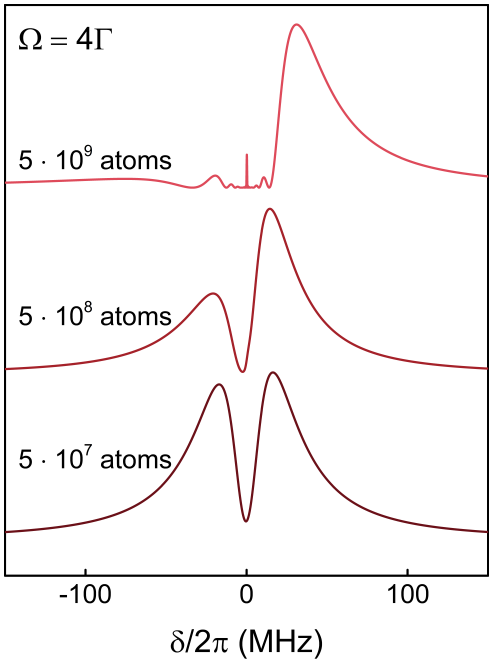

Figure 35 – Theoretical FWM spectra for three numbers of atoms in the MOT with the phase matching taken into account. The Rabi frequency of each input beam is Ω. All curves are normalized.

the spectrum is completely different. For this situation the $sinc^2(\Delta kL)$ function oscillates near the resonance destroying the red-shifted part of the spectrum. Furthermore, this lack of robustness in the line shape contradicts the experimental results presented in section 3.3.

On the other hand, for slightly smaller N, there is an asymmetry that almost resembles the experimental FWM spectrum, but in the other direction, i.e. in the experiment the higher peak appears for smaller frequencies. At this point, the full elucidation of this asymmetry remains open. If it is due to the phase matching condition, then the fluorescence measurements of the number of atoms are inaccurate and the peak relation in the experimental spectrum should also be mistaken. The other option to be explored, which has more evidences giving support, is the temporal dynamics discussed with the experimental results of section 3.6, for which we still do not have a model.

4.5 Comparison with the literature

Although we have found no reports in the literature of FWM experiments in the same conditions of ours, especially in this single laser setup, it is important to compare our model with the closest results available. The typical experiments use a strong beam with a fixed frequency and a weak beam that probes the system by scanning the frequency. This type of condition cannot be reproduced in our experiment, but it is easily done in the model.

In this context, the result of Fig. 36 presents the comparison between the direct and the complete solution with the beam a fixed on resonance and scanning the beam b. This latest has

a Rabi frequency an order smaller than Γ. Absorption effects were neglected on this result, so it uses the same model of Fig. 29. The curves have several interesting features. To begin with, as the intensity of the beam *a* increases there is a splitting of the signal. This type of effect is consistent with an Autler-Townes splitting, since the distance between the peaks scales with the intensity and they are clearly defined. This means then, that in this type of situation, the beam *a* is strong enough to cause an AC Stark effect that breaks the involved levels in two.

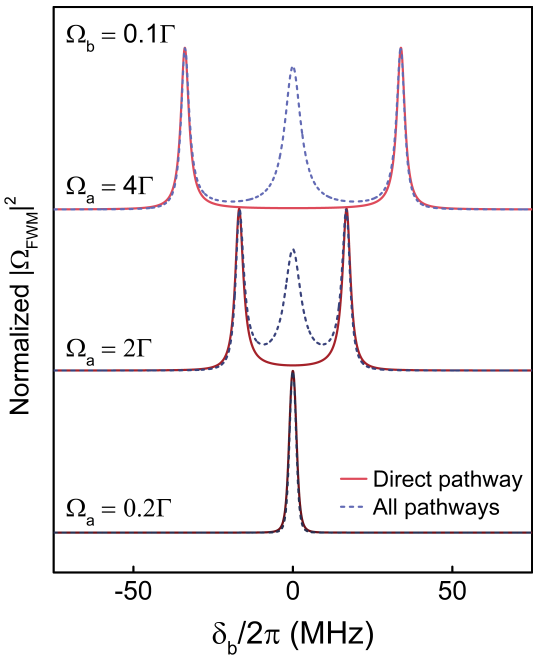

Figure 36 – Theoretical results for the FWM signal with a strong fixed beam (*a*) and scanning probe beam (*b*) for three intensities of the input lasers using the complete solution (blue) and only the direct pathway (red). Absorption effects were neglected. All curves are normalized.

In addition, both solutions give identical results, with the exception of the central peak in the complete solution. In fact, this type of triplet structure was seen by Lezama *et al* in a study of the near degenerate FWM in a phase conjugation experiment with cold cesium atoms [34]. In this work they present theory and experiment for pure two-level FWM process using counter-propagating beams alongside a probe beam with the frequency being scanned. Although, the experimental conditions are quite different, the result in Fig. 36 presents some similarity with the ones of Lezama *et al* [34], especially the complete solution with the triplet structure. This reinforces the idea that the core of our model is in fact in the right direction. On the other hand, the different experimental conditions allow us to use only the direct solution, the one that presents some agreement the experimental result.

Finally, this comparison might give insight on the reason the complete solution does not present a consistent valley when both beams are being scanned simultaneously, even including all absorption effects (see Fig. 33). From a purely mathematical point of view, it seems that this central peak of the complete solution is precisely what prevents the arising of the valley. Notice

that when we scan both beams, it is not possible to see this intensity splitting of Fig. 36, so all peaks stay together at the center. Being this the case, the real part of the Rabi frequency Ω_{FWM} cannot overcome the imaginary part if all four excitation pathways are considered.

The most important question at this point is to elucidate the physical differences between our setup, with both input beams being scanned, and the typical setup with only a probe beam scanning the system. One possibility is that, since our lasers always have the same frequencies simultaneously, the coherence between the ground states of the system (see Fig. 27) should last much longer than it would last in a situation with a fixed frequency laser. This seems to be the reason why there is not a intensity splitting (Autler-Townes effect) in all previous theoretical results with both scanning beams, because the equal detuning of the input beams eliminate resonances in Eq. (71). The question remaining is if this physical difference, or any other that the system might have, is enough to justify dropping out three of the four excitation pathways that arise from the model.

5 CONCLUSIONS

We have successfully performed an experiment to study the FWM process using atoms cooled by a MOT, in a copropagating configuration of the input beams. In fact, the experiment was designed in such a way to generate two FWM signals in distinct directions. In a first attempt to analyze the correlations between these two signals, the setup consisted of two separate cw lasers allowing a preliminary description of the correlations. The Pearson coefficient of over 90% indicates a strong positive correlation between the two FWM processes.

Given the experimental difficulties of the two lasers setup, most of the experimental data of this work were taken using a single laser. This allows easier and more trustworthy measurements. Under this configuration the FWM spectrum presented an unexpected valley around the resonance. To achieve the correct interpretation of this valley became one of the central goals of this research. In section 3.2 we showed that varying the intensity of the input beams only introduces a power broadening in the FWM signal, but does not seem to affect deeply the shape and width of the valley. In fact, the experimental range of intensity of the input beams went from two orders below to two orders above saturation intensity resulting in no significant change. A more detailed analysis revealed that around the saturation intensity the valley depth does decrease by a factor of 10%.

The main hypotheses to explain such a valley in the FWM spectrum were, before formulating the theoretical model, weakened by the experimental evidences. The shape and width of the valley already discarded the possibility of a enhanced absorption due to the coherent interaction of the atoms with the beams, i.e. an electromagnetically induced absorption, since this phenomenon presents a much narrower absorption. The robustness of the valley and the fact that for high intensities there was no clear separation between the two peaks ruled out the splitting of atomic levels due to AC Stark effect, i.e. an Autler-Townes splitting.

Finally, the mere absorption of the input beams and the generated signal should not be enough to produce such a deep valley in a high intensity regime. Changing the optical density of the atomic sample (see section 3.3) confirmed that the valley should not be completely due to absorption effects, since a low density sample rendered the same usual FWM spectrum.

Others parameters of the system were studied as well. For example, we added an external magnetic field to the experimental setup, which did not provoke any significant change because the maximum field produced was not strong enough. We have as well studied the effect of the scanning ramp direction and speed in the FWM signal. This measurement shows that there is some temporal dynamics induced by the fast scanning beams, which changes the symmetry of the FWM spectrum.

To further confirm the existence of this temporal dynamics, we plan to perform the

experiment acquiring one point of data per time window, as described in chapter 2. To use such a technique, we must first lock the frequencies of the cooling and repump beams of the MOT. It will be necessary as well to use an AOM to control the input beams. If there is in fact some temporal dynamics, we expect that the results from this measurement will have no asymmetry since there will be no fast scans of the laser frequency.

To achieve an interpretation of the features of the FWM signal, we have modeled the process as described in chapter 4. The model gives evidence that absorption effects are only capable to explain the experimental results for a low intensity regime, as expected. For high intensities of the input beams, the real part of the Rabi frequency of the generated FWM light dominates the spectrum, and therefore dispersion is the phenomenon that explains the valley. However, the model does not achieve a perfect description of the experimental data, especially around the saturation intensity where the theoretical valley depth has a 60% fall, against the 10% fall in the experiment.

Furthermore, the model cannot achieve a description of the asymmetry in the FWM spectrum. The phase matching condition could introduce an asymmetry but only for less dense samples and with an inadequate peak relation. It remains open then, if the temporal dynamics induced by the fast scans can be the source of the asymmetry. If this is the case, then it is necessary to somehow change the model to take into account this dynamics.

Finally, it is fundamental to find a solid physical argument that justifies using only the direct pathway of excitation in the model. In chapter 4 we showed that this direct solution achieves a much better agreement with the experimental results. We must emphasize that, even though the other three routes have eccentric excitation orders, they still are natural consequences of the perturbation solution. There must be a physical justification to drop out these terms.

Once the open questions of this work, regarding both experiment and theory, are answered, we expect to perform these measurements using beams with orbital angular momentum. This should introduce some imbalance between the input beams, that were for all aspects identical in this work, and as a consequence affect the two FWM process. This experiment should have interesting results, and all the techniques and analyses presented here will be useful for this future research.

REFERENCES

1 ASHKIN, A. History of optical trapping and manipulation of small-neutral particle, atoms, and molecules. *IEEE Journal of Selected Topics in Quantum Electronics*, v. 6, n. 6, p. 841–856, 2000. Cited on page 11.

2 DENG, L. et al. Four-wave mixing with matter waves. *Nature*, v. 398, p. 218–220, 1999. Cited on page 11.

3 XIAO-SONG, L. et al. Generation of a non-classical correlated photon pair via spontaneous four-wave mixing in a cold atomic ensemble. *Chinese Physics Letters*, v. 26, n. 6, p. 064204, 2009. Cited on page 11.

4 DUDIN, Y. O.; KUZMICH, A. Strongly interacting rydberg excitations of a cold atomic gas. *Science*, v. 336, p. 887–889, 2012. Cited on page 11.

5 BORBA, G. C.; FELINTO, D.; TABOSA, J. W. R. Nonlinear optical memory: theory and experiment. *Journal of the Optical Society of America B*, v. 34, n. 12, p. 2528–2537, 2017. Cited on page 11.

6 MAIMAN, T. H. Stimulated optical radiation in ruby. *Nature*, v. 187, p. 493–494, 1960. Cited on page 12.

7 FRANKEN, P. A. et al. Generation of optical harmonics. *Physical Review Letters*, v. 7, p. 118–119, 1961. Cited on page 12.

8 KAISER, W.; GARRETT, G. C. B. Two-photon excitation in CaF_2; Eu^{2+}. *Physical Review Letters*, v. 7, p. 229–231, 1961. Cited 2 times on pages 12 e 15.

9 WOODBURY, E. J.; NG, W. K. Ruby laser operation in the near ir. *Proceedings of the IRE*, v. 50, p. 2347–2348, 1962. Cited on page 12.

10 MAKER, P. D.; TERHUNE, R. W. Optical third harmonic generation. *Journal of the Optical Society of America*, v. 53, p. 523, 1963. Cited on page 12.

11 THE Nobel Prize in Physics 1981. 2019. Nobel Media AB. Available from Internet: <https://www.nobelprize.org/prizes/physics/1981/press-release/>. Accessed on: 10 jan 2019. Cited on page 12.

12 MORENO, M. P.; ALMEIDA, A. A. C. de; VIANNA, S. S. Coherent blue light driven by a diode laser and a high repetition rate pulse train. *Frontiers in Optics / Laser Science*, p. JTu2A.7, 2018. Cited on page 12.

13 BOYER, V. et al. Entangled images from four-wave mixing. *Science*, v. 321, p. 544–547, 2008. Cited on page 12.

14 DEN, W.; STRICKLER, J. H.; W.W.WEBB. Two-photon laser scanning fluorescence microscopy. *Science*, v. 248, p. 4951, 1990. Cited on page 12.

15 BOYD, R. *Nonlinear Optics*. 3. ed. Orlando, FL, USA: Academic Press, 2008. Cited 2 times on pages 12 e 51.

16 HäNSCH, T. W.; SHAHIN, I. S.; SCHAWLOW, A. L. High-resolution saturation spectroscopy of the sodium d lines with a pulsed tunable dye laser. *Physical Review Letters*, v. 27, p. 707, 1971. Cited on page 15.

17 THE Nobel Prize in Physics 1997. 2019. Nobel Media AB. Available from Internet: <https://www.nobelprize.org/prizes/physics/1997/summary/>. Accessed on: 16 jan 2019. Cited on page 15.

18 FOOT, C. J. *Atomic Physics (Oxford Master Series in Physics)*. 1. ed. Oxford, UK: Oxford University Press, 2005. Cited 2 times on pages 15 e 17.

19 CHU, S. et al. Three-dimensional viscous confinement and cooling of atoms by resonance radiation pressure. *Physical Review Letters*, v. 55, p. 48, 1985. Cited on page 15.

20 WALLACE, C. D. et al. Measurements of temperature and spring constant in a magneto-optical trap. *Journal of the Optical Society of America B*, v. 11, n. 5, p. 703–711, 1994. Cited on page 16.

21 RAAB, E. L. et al. Trapping of neutral sodium atoms with radiation pressure. *Physical Review Letters*, v. 59, p. 2631, 1987. Cited on page 17.

22 STEANE, A. M.; CHOWDHURY, M.; FOOT, C. J. Radiation force in the magneto-optical trap. *Journal of the Optical Society of America B*, v. 9, n. 12, p. 2142–2158, 1992. Cited on page 18.

23 SCHERER, D. R.; FENNER, D. B.; HENSLEY, J. M. Characterization of alkali metal dispensers and non-evaporable getter pumps in ultrahigh vacuum systems for cold atomic sensors. *Journal of Vacuum Science & Technology A*, v. 30, p. 061602, 2012. Cited on page 19.

24 VEISSIER, L. *Quantum memory protocols in large cold atomic ensembles*. Thesis (Phd) — Université Pierre et Marie Curie - Paris VI, Paris, France, 2013. Available from Internet: <https://tel.archives-ouvertes.fr/tel-00977307/document>. Accessed on: 17 jan. 2019. Cited on page 19.

25 PALITTAPONGARNPIM, P. *Characterization of Magneto-optical Trap For Experiments in Light-Atom Interfacing*. Dissertation (Master's thesis) — University of Calgary, 2012. Cited on page 23.

26 STECK, D. A. *Rubidium 87 D Line Data*. 2003. Available from Internet: <https://steck.us/alkalidata/rubidium87numbers.1.6.pdf>. Accessed on: 17 jan 2019. Cited 4 times on pages 27, 37, 50 e 54.

27 PEARSON correlation coefficient. 2019. Wikipedia, the free encyclopedia. Available from Internet: <https://en.wikipedia.org/wiki/Pearson_correlation_coefficient>. Accessed on: 18 jan 2019. Cited on page 30.

28 AUTLER, S. H.; TOWNES, C. H. Stark effect in rapidly varying fields. *Physical Review*, v. 100, p. 703, 1955. Cited on page 31.

29 BABIN, S. A. et al. Level-splitting effects in resonant four-wave mixing. *Optics Letters*, v. 26, n. 2, p. 81–83, 2001. Cited on page 31.

30 LEZAMA, A.; BARREIRO, S.; AKULSHIN, A. M. Electromagnetically induced absorption. *Physical Review A*, v. 59, n. 6, p. 4732, 1998. Cited on page 31.

31 GOREN, C. et al. Electromagnetically induced absorption due to transfer of coherence and to transfer of population. *Physical Review A*, v. 67, p. 033807, 2003. Cited on page 32.

32 OLIVEIRA, M. D. F. A. M. de; BLOCH, D. Theory of resonant doppler-broadened backward four-wave mixing in the pump saturation regime. *Physical Review A*, v. 32, p. 1614, 1985. Cited on page 51.

33 YARIV, A. *Quantum Electronics*. 3. ed. Hoboken, NJ, USA: John Wiley & Sons, 1989. Cited on page 52.

34 LEZAMA, A.; CARDOSO, G. C.; TABOSA, J. W. R. Polarization dependence of four-wave mixing in a degenerate two-level system. *Physical Review A*, v. 63, p. 013805, 2000. Cited on page 59.